Finite Elements in Analysis and Design 258 (2026) 104551

Contents lists available at ScienceDirect

Finite Elements in Analysis & Design

journal homepage: www.elsevier.com/locate/finel

3D numerical modeling of glioblastoma cells progression in microfluidic devices

E. Sala-Lardies [a], J. Sarrate [a,*], M. Pérez-Aliacar [b], J. Ayensa-Jiménez [b,c], M. Doblaré [b,d,e], N. Parés [a]

[a] Laboratori de Càlcul Numèric (LaCàN), Universitat Politècnica de Catalunya - Barcelona-Tech (UPC), Jordi Girona 1-3, Barcelona, 08024, Spain
[b] TME Lab, Aragón Institute of Engineering Research (I3A), University of Zaragoza, Mariano Esquillor s/n, Zaragoza, 50018, Spain
[c] Institute for Health Reearch Aragon (IISA), Avenida San Juan Bosco, 13, Zaragoza, 50009, Spain
[d] CIBER-BBN, ISCIII, Monforte de Lemos 3-5, Madrid, 28029, Spain
[e] Sino-Spain Joint Laboratory on Biomedical Materials (S2BLM), College of Materials Science and Engineering Nanjing Tech University, 5 Xinmofan Rd, Gu Lou Qu, Nanjing Shi, 210037, China

ARTICLE INFO

Keywords:
Glioblastoma (GBM)
High-order continuous Galerkin
High-order diagonally implicit Runge–Kutta
Newton method

ABSTRACT

Mathematical and computational models provide a powerful framework for understanding complex biological processes such as cancer cell progression. Here, we present a numerical formulation for the simulation of the evolution of glioblastoma (GBM) cancer cells in microfluidic devices which are commonly used to replicate the dynamic changes of the tumor cells in a biomimetic microenvironment. We model this physicochemical and biological complexity with a coupled nonlinear system of transient partial differential equations involving different chemical species and cell phenotypes. In particular, we consider oxygen as the main chemical driver and the concentration of two cell phenotypes: living and dead cells. The system is solved combining a high-order continuous Galerkin finite element formulation in space with a high-order diagonally implicit Runge–Kutta (DIRK) scheme in time. This leads to a coupled nonlinear system for oxygen and living cells at each stage of the DIRK scheme that we solve using the Newton method. The same integration method is used to solve for dead cells at each mesh node. Finally, we present several examples to assess and illustrate the capabilities of the proposed formulation. The results demonstrate that this model is a valuable tool for advancing our understanding of cancer cell progression and for supporting the industrial design of novel devices aimed at testing new hypotheses and guiding experimental research.

1. Introduction

Glioblastoma (GBM) is the most common of the primary brain tumors, accounting for an incidence of 17% within that family of cancers. Moreover, it is also the most aggressive and lethal of the brain tumors, with a median survival of 14 months since diagnosis and a 5-year survival rate of less than 10% [1,2]. That poor prognosis is due to its rapid growth and the surgical limitations for its complete resection, even with the new advanced neuroimaging and intra-operative techniques [3].

GBM cells are integrated in a complex, heterogeneous, and extremely dynamic microenvironment that prevents the use of *in vivo* experiments to control and isolate the effects of a particular variable or phenomenon. *In vitro* experiments have been intensely used

* Corresponding author.
E-mail address: jose.sarrate@upc.edu (J. Sarrate).
URL: http://www-lacan.upc.edu (J. Sarrate).

https://doi.org/10.1016/j.finel.2026.104551
Received 18 November 2025; Received in revised form 6 March 2026; Accepted 12 March 2026
Available online 11 April 2026
0168-874X/© 2026 The Authors. Published by Elsevier B.V. This is an open access article under the CC BY-NC-ND license (http://creativecommons.org/licenses/by-nc-nd/4.0/).

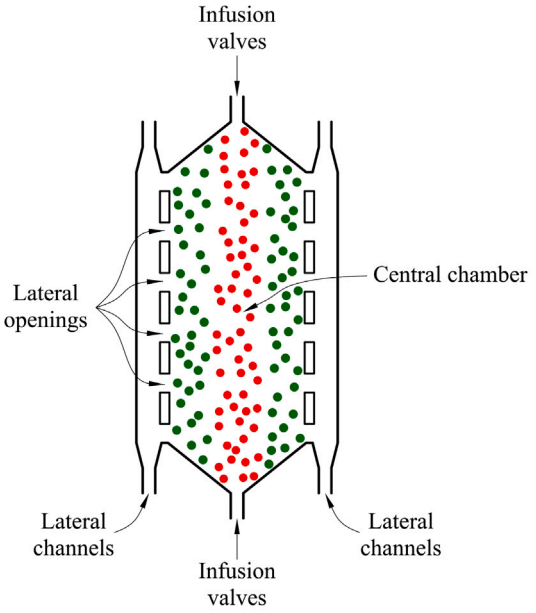

Fig. 1. 2D sketch of a microfluidic device. It is composed of a central chamber that initially contains a mixture of collagen hydrogel, oxygen, and living GBM cells that are seeded through two infusion valves. Two lateral channels are used to supply oxygen to the mixture via several lateral openings.

to better control some of these variables and recreate part of the GBM microenvironment complexity. However, the predictive and analytical power of these experiments is still limited and expensive, both from the point of view of human and material resources. In addition, fundamental aspects such as the three-dimensional character of GBM microenvironment structure are largely lost when using standard Petri dishes [4]. The advent of microfluidic devices [5,6] has made it possible to overcome some of these limitations, allowing greater control over many system parameters and providing temporal flexibility that is difficult to achieve in conventional 2D or 3D culture systems [7].

The microfluidic devices considered here [8–10] are composed of a central chamber connected to two lateral microchannels via one or several lateral openings, see Fig. 1. These devices have been fabricated using cyclic olefin polymer (COP) which makes their walls impermeable to liquids and gases. Also, their shape and dimensions may vary depending on the type of experiment to be carried out. A mixture of collagen hydrogel, oxygen, and living GBM cells is inserted into the central chamber using two infusion or inlet valves located at the upper and lower part of the central chamber. Once this process is ended, the valves are closed maintaining the impermeability. To analyze the behavior of the GBM cells under different conditions, a growth medium rich in oxygen is perfused along the lateral microchannels. For instance, Fig. 1 depicts the case in which oxygen is supplied from both lateral channels. Consequently, living GBM cells (depicted as green circles), once they have consumed the oxygen present in the surrounding hydrogel, either migrate towards the lateral channels generating two palisades with a high concentration of GBM living cells next to the lateral channels, or they perish (become dead cells depicted as red circles) generating a necrotic core in the central part of the chamber.

The time required to generate the palisades, as well as the location, shape and maximum value of the concentration of living cells, has been found to strongly depend on the dimensions of the device, the initial concentration of oxygen and living cells of the infused mixture, as well as the oxygen concentration of the perfused growth medium through the lateral channels [8–12]. Therefore, an *in silico* tool would assist engineers during the design process of these microfluidic devices and experiments to expand their potential, and would guide biologists and biomedical experimentalists to acquire new insights into GBM progression dynamics, and predict the outcome of new hypotheses.

This work presents three basic contributions. First, it extends to a multidimensional setting the mathematical model presented in [11] for the simulation of GBM cells. When considering two cell phenotypes (living and dead cells) and one nutrient (oxygen), the resulting system comprises two coupled nonlinear partial differential equations (PDE) governing oxygen and living cells behavior along with a coupled PDE for dead cells. Note that we only consider dead cells to monitor their spatial concentration over time. Since there is no motion for dead cells, their evolving equation does not involve spatial derivatives and it reduces to a family of ordinary differential equations (ODE), one for each fixed spatial point. The second contribution relies on developing a high-order formulation, both in time and space, to solve these equations. High-order methods are well-suited to solve this type of problems [13–15]. For example, using elements of degree p, a convergence rate of $p+1$ is expected, offering a high accuracy even with coarse meshes. In time, diagonally implicit Runge–Kutta (DIRK) schemes are employed to achieve high-order accuracy for the

integration procedure [16–19]. Finally, the third contribution consists of the successful application of the developed formulation to industrial microfluidic devices.

The outline of the paper is as follows. Section 2 introduces the general formulation of our mathematical model and particularizes it to the specific problem of the GBM cell progression in microfluidic devices. In Section 3 we detail the numerical approach proposed to solve the coupled nonlinear problems by means of a high-order formulation and Newton method. Section 4 analyzes several examples that assess the reliability of the proposed formulation. Finally, in Section 5 we summarize the main contributions of our work and outline several aspects that will be addressed in the near future.

2. Mathematical model

In this section, we first introduce the general mathematical model for GBM evolution in microfluidic devices. Then, we particularize it to the purposes of this work, providing a detailed description of the specific parameters for the model.

2.1. General governing equations

Let $\Omega \subset \mathbb{R}^d$, with $d = 2$ or 3, be the physical domain representing the central chamber of the microfluidic device, with Lipschitz boundary $\partial\Omega$, and let $I = (0, T)$ be the time interval of interest. This central chamber is infused with a mixture of collagen hydrogel, n_1 chemical specimens (such as nutrients or drugs), and n_2 cell populations (including different cell phenotypes of GBM cells). The concentrations of chemical species and cell populations are denoted by $c^i(\boldsymbol{x}, t)$, where $\boldsymbol{x} \in \Omega$ and $t \in [0, T]$, for $i = 0, \dots, n-1$, with $n = n_1 + n_2$. The first n_1 correspond to nutrients or drugs, while the remaining n_2 correspond to different cell phenotypes. Let also $\boldsymbol{c} = [c^0, c^1, \dots, c^{n-1}]^T$ denote the vector containing all concentrations.

The evolution of the concentration of these chemical specimens and GBM cells in the microfluidic device is modeled by the following transport equation:

$$\frac{\partial c^i}{\partial t} + \boldsymbol{\nabla} \cdot \boldsymbol{f}^i = s^i \qquad \text{for } i = 0, 1, \dots, n-1. \tag{1}$$

Here, $\boldsymbol{f}^i$ and s^i represent the vector-valued flux and scalar source term associated with the concentration $c^i(\boldsymbol{x}, t)$. Both $\boldsymbol{f}^i$ and s^i are nonlinear functions of concentrations, that is, $s^i(\boldsymbol{x}, t; \boldsymbol{c})$ and $\boldsymbol{f}^i(\boldsymbol{x}, t; \boldsymbol{c})$, although this dependency is omitted in the rest of the paper for simplicity of presentation.

We consider that the motion of the chemical species in the hydrogel is assumed to be driven solely by diffusion [20]. Thus, there is no convective term for them, so the corresponding fluxes are given by:

$$\boldsymbol{f}^i = -\boldsymbol{A}^i \boldsymbol{\nabla} c^i \qquad \text{for } i = 0, \dots, n_1 - 1, \tag{2}$$

where $\boldsymbol{A}^i$ are the diffusion matrices. In general, these matrices may be nonlinear functions of the cell concentration $\boldsymbol{A}^i(\boldsymbol{x}, t; \boldsymbol{c})$.

The motion of cell phenotypes is driven by diffusion processes (pedesis term for random cell migration) and a chemotaxis convective term proportional to the local gradient of the chemical species, [20,21]. Consequently, the fluxes are modeled as follows:

$$\boldsymbol{f}^i = -\boldsymbol{A}^i \boldsymbol{\nabla} c^i + \sum_{j=0}^{n_1-1} c^i \boldsymbol{B}^{ij} \boldsymbol{\nabla} c^j \qquad \text{for } i = n_1, \dots, n-1. \tag{3}$$

Here, $\boldsymbol{A}^i$ and $\boldsymbol{B}^{ij}$ are the diffusion and chemotaxis matrices, respectively. Similar to the motion of chemical species, these matrices are generally nonlinear functions of cell concentrations, namely, $\boldsymbol{A}^i(\boldsymbol{x}, t; \boldsymbol{c})$ and $\boldsymbol{B}^{ij}(\boldsymbol{x}, t; \boldsymbol{c})$. This dependency will be also explicitly omitted for simplicity. It should be noted that, from a mathematical point of view, Eq. (2) can be considered a particular case of Eq. (3) with $\boldsymbol{B}^{ij} = \boldsymbol{0}$, although they have been formulated from different physical phenomena.

The source terms for chemical species and cell phenotypes are modeled as follows:

$$s^i = -\sum_{j=0}^{n_1-1} \beta^{ij} c^j - \sum_{j=n_1}^{n-1} \alpha^{ij} c^j \qquad \text{for } i = 0, \dots, n_1 - 1, \tag{4}$$

$$s^i = \frac{1}{\tau^{ii}} c^i - \sum_{\substack{j=n_1 \\ j \neq i}}^{n-1} \frac{1}{\tau^{ij}} c^i + \sum_{\substack{j=n_1 \\ j \neq i}}^{n-1} \frac{1}{\tau^{ji}} c^j \qquad \text{for } i = n_1, \dots, n-1. \tag{5}$$

Here, β^{ij} represents the reaction rate from the ith chemical specimen to the jth chemical specimen, while α^{ij} denotes the rate of the ith chemical specimen consumed by the jth cell phenotype. The parameter τ^{ii} is the characteristic time of proliferation for the ith population, and τ^{ij} is the characteristic time of differentiation from population i to j.

The matrices and coefficients involved in the model, namely $\boldsymbol{A}^i, \boldsymbol{B}^{ij}, \beta^{ij}, \alpha^{ij}, \tau^{ii}$ and τ^{ij}, may depend on mechanical cues such as hydrogel stiffness or local strain and on the temperature distribution. However, as discussed in [11,12], we assume that these quantities are either constant or dependent only on the concentration of GBM cells and chemical specimens. Consequently, we consider $\alpha^{ij}(\boldsymbol{c})$ with similar dependencies assumed for the remaining quantities. For simplicity, this dependency is omitted throughout the paper.

Eq. (1) is completed with proper initial and boundary conditions as follows:

$$\left.\begin{aligned} c^i(\boldsymbol{x},0) &= c^{i,0}(\boldsymbol{x}) && \text{in } \Omega \\ c^i(\boldsymbol{x},t) &= g_D^i && \text{on } \Gamma_D^i \\ \boldsymbol{f}^i\cdot\boldsymbol{n} &= g_N^i && \text{on } \Gamma_N^i \\ \boldsymbol{f}^i\cdot\boldsymbol{n} &= \gamma^i(c^i - g_R^i) && \text{on } \Gamma_R^i \end{aligned}\right\} \quad \text{for } i = 0,\dots,n-1. \tag{6}$$

Here, for each specimen, the boundary $\partial\Omega$ is divided into three disjoint parts: Dirichlet boundary, Γ_D^i, Neumann boundary, Γ_N^i, and Robin boundary, Γ_R^i, such that $\partial\Omega = \bar{\Gamma}_D^i \cup \bar{\Gamma}_N^i \cup \bar{\Gamma}_R^i$. Both the initial condition $c^{i,0}(\boldsymbol{x})$ and the data associated with the boundary conditions g_D^i, g_N^i and g_R^i are assumed to be sufficiently smooth, and γ^i is a boundary parameter to be fitted.

Finally, we note that different mathematical models and numerical formulations have been proposed in the literature to describe the growth of cancer cells. For instance, in [22,23] the growth of the glioblastoma is modeled using a Cahn-Hilliard–type equation and a finite element formulation is used to solve it. In addition, [24,25] present a reaction–diffusion formulation with a phase-field variable to account for the prostate tumor growth, which is solved using meshless methods combined with a first-order time scheme. The progression of prostate cancer is also modeled in [26] using a phase-field model coupled with chemotherapy and antiangiogenic therapy that is solved using the isogeometric discretization and a second-order time scheme.

2.2. 3D specific model with two cell phenotypes and one chemical species

In this section, we adapt the general formulation introduced earlier to a specific model for GBM progression in microfluidic devices. Although the previous formulation considers a broader range of scenarios, the model presented here is tailored to reproduce several working experiments showing the main GBM structures (living cell palisade and necrotic core formation).

Although other studies have considered a larger number of phenotypes [8,10,27], we follow the approach in [11,12] and consider two phenotypes of GBM cells: living cells, $c^1(\boldsymbol{x},t)$, and dead cells, $c^2(\boldsymbol{x},t)$. This choice is motivated by the assumption that all GBM cells in our experiments respond similarly to the same stimuli, in line with experimental evidence suggesting that GBM cells do not necessarily maintain fixed phenotypic identities but rather undergo dynamic and reversible transitions in response to environmental cues within the tumor microenviromental niche such as local hypoxia. In this sense, the differences in proliferation, differentiation and migration primarily depend on the local properties of the surrounding environment [28].

In addition, based on previous works [29,30] and also supported by the experiments presented in [9,10], we consider oxygen to be the primary driver that regulates the GBM progression. The experiments demonstrated that the distribution of other nutrients, such as glucose, does not significantly influence cell configuration, reinforcing oxygen as the main stimulus for cell behavior [29,30]. Furthermore, since no drugs are supplied during the experiments, oxygen, denoted by $c^0(\boldsymbol{x},t)$, is the only chemical species included in our specific model.

Fig. 2 shows a sketch of the central chamber of a microfluidic device Ω and the decomposition of its boundary. The boundary $\partial\Omega$ is divided into three disjoint parts, $\partial\Omega = \bar{\Gamma}^{\text{in}} \cup \bar{\Gamma}^{\text{op}} \cup \bar{\Gamma}^{\text{sw}}$: the inlet valves Γ^{in}, the lateral openings Γ^{op}, and the solid walls Γ^{sw}. Inlet valves are used to infuse the mixture of collagen and GBM cells, while lateral openings allow oxygen supply. The remaining boundaries are impermeable solid walls that prevent cell and oxygen exchange. Note that once the mixture is infused, the inlet valves are closed and behave as impermeable solid walls.

With these assumptions, we are ready to pose the specific mathematical equations describing the evolution of the concentration of oxygen, living cells, and dead cells, recalling that in this case, we have $n_1 = 1$, $n_2 = 2$ and therefore $n = 3$ and $\boldsymbol{c} = [c^0, c^1, c^2]^T$.

Oxygen. The governing equation for the concentration of oxygen, $c^0(\boldsymbol{x},t)$, is obtained by particularizing Eqs. (1), (2) and (4) to the current model:

$$\frac{\partial c^0}{\partial t} + \boldsymbol{\nabla}\cdot\boldsymbol{f}^0 = s^0 \quad \text{for} \quad \boldsymbol{f}^0 = -\boldsymbol{A}^0\boldsymbol{\nabla}c^0 \quad \text{and} \quad s^0 = -\beta^{00}c^0 - \alpha^{01}c^1 - \alpha^{02}c^2.$$

Several works [11,31,32] consider constant oxygen diffusion, although our model can account for heterogeneous diffusion $\boldsymbol{A}^0(\boldsymbol{x},t;\boldsymbol{c}) = \boldsymbol{A}^0(\boldsymbol{x})$. To model oxygen consumption, the source term is derived by setting $\beta^{00}(\boldsymbol{c}) = 0$ because the oxygen natural decay is much slower than the cell oxygen consumption [8,11,33]. In addition, we set $\alpha^{02}(\boldsymbol{c}) = 0$, since dead cells do not consume oxygen. The oxygen uptake by living cells, present in the model via the variable $\alpha^{01}(\boldsymbol{c})$, is modeled using a Michaelis–Menten kinetics model [8,9,11]. With these assumptions, the source term for the oxygen equation becomes

$$s^0(\boldsymbol{c}) = -\alpha^{01}(\boldsymbol{c})c^1 = -\alpha_*^{01}\, r(c^0;c_m^0)\, c^1, \tag{7}$$

where α_*^{01} is a constant oxygen consumption rate, and

$$r(c^0;c_m^0) = \frac{c^0}{c^0 + c_m^0}, \tag{8}$$

being c_m^0 is the Michaelis–Menten constant, representing the oxygen concentration at which the reaction rate is half of the rate in a fully oxygenated medium.

To complete the oxygen model, appropriate boundary conditions are prescribed to reflect the physical characteristics of the microfluidic device. On the inlet valves and on the solid walls of the central chamber, which are impermeable, we impose homogeneous Neumann boundary conditions to model zero flux across these boundaries. This corresponds to $\Gamma_N^0 = \Gamma^{\text{sw}} \cup \Gamma^{\text{in}}$ and $g_N^0 = 0$ in Eq. (6). On the lateral openings, where oxygen is supplied, we prescribe Dirichlet boundary conditions to account

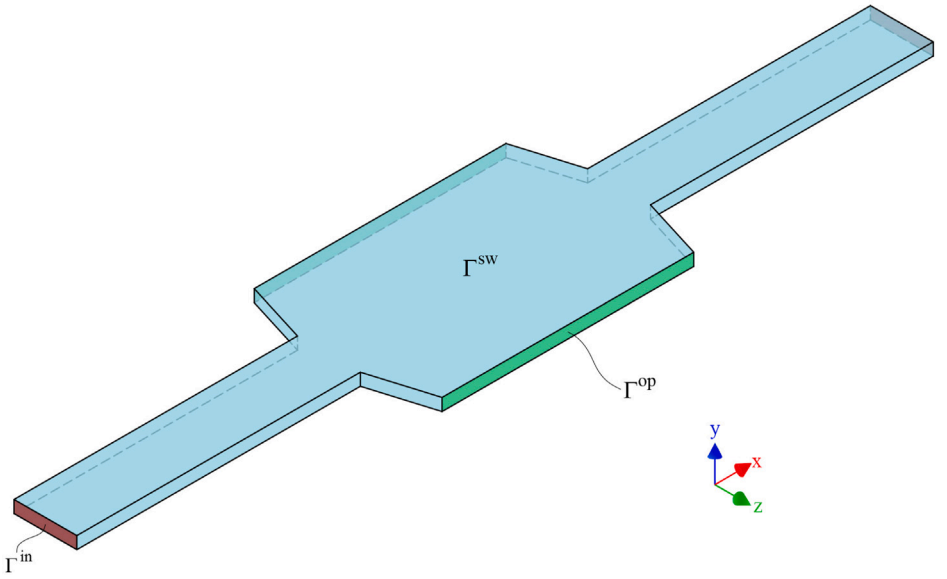

Fig. 2. Sketch of a 3D microfluidic device with its boundary decomposition: inlet valves Γ^{in} in brown, lateral openings Γ^{op} in green and solid walls Γ^{sw} in blue.

for the controlled oxygen concentration in the adjacent channels. Specifically, we set $\Gamma_D^0 = \Gamma^{op}$, where the value of g_D^0 depends on the experimental conditions being modeled. Finally, since no Robin boundary conditions are considered, we set $\Gamma_R^0 = \emptyset$.

Living cells. The governing equation for the concentration of living cells, $c^1(\boldsymbol{x}, t)$, is obtained by particularizing Eqs. (1), (3) and (5) to the current model:

$$\frac{\partial c^1}{\partial t} + \nabla \cdot \boldsymbol{f}^1 = s^1 \quad \text{for} \quad \boldsymbol{f}^1 = -\boldsymbol{A}^1 \nabla c^1 + c^1 \boldsymbol{B}^{10} \nabla c^0 \quad \text{and} \quad s^1 = \frac{1}{\tau^{11}} c^1 - \frac{1}{\tau^{12}} c^1 + \frac{1}{\tau^{21}} c^2.$$

To model the evolution of living cells, we consider the go-or-grow paradigm [34], where cells alternate between proliferation or migration depending on environmental conditions. Specifically, the motility of living cells described via the flux term $\boldsymbol{f}^1(\boldsymbol{c})$ is defined based on two key mechanisms:

- Diffusion: Living cells undergo a standard Fickian diffusion process with a homogeneous diffusion matrix, $\boldsymbol{A}^1(\boldsymbol{x}, t; \boldsymbol{c}) = \boldsymbol{A}^1$ [11,31,32].
- Chemotaxis: Living cells obey a chemotaxis process that responds to both oxygen availability (migrating only if oxygen saturation is below a critical threshold) and space availability (moving only if the local environment is not saturated) [35,36].

According to [11,12], the chemotaxis matrix $\boldsymbol{B}^{10}(\boldsymbol{c})$ is modeled as

$$\boldsymbol{B}^{10}(\boldsymbol{c}) = \boldsymbol{B}_*^{10} \psi_-(c^0; c_h^0) \psi_-(c^1; c_s^1), \tag{9}$$

where $\boldsymbol{B}_*^{10}$ is the constant chemotaxis matrix, c_h^0 is the hypoxia migration threshold, and c_s^1 is the cell saturation threshold while the deactivation rectified linear unit (ReLU) function, $\psi_-(x; \theta)$, is defined as follows:

$$\psi_-(x; \theta) = \begin{cases} 1 & \text{if } x < 0, \\ 1 - x/\theta & \text{if } 0 \le x \le \theta, \\ 0 & \text{if } x > \theta. \end{cases} \tag{10}$$

The source term associated with living cells, $s^1(\boldsymbol{c})$, is derived by considering dead cells as inert material. Consequently, the term containing $\tau^{21}(\boldsymbol{c})$ is not present in the model. Thus, the growth of living cells is governed solely by the characteristic time of proliferation $\tau^{11}(\boldsymbol{c})$ and the characteristic time of differentiation $\tau^{12}(\boldsymbol{c})$, namely

$$s^1(\boldsymbol{c}) = \frac{1}{\tau^{11}(\boldsymbol{c})} c^1 - \frac{1}{\tau^{12}(\boldsymbol{c})} c^1. \tag{11}$$

For the proliferation process, we consider that it depends on oxygen and space availability. Specifically, GBM cells proliferate if the oxygen concentration is above a hypoxic threshold and if the saturation of living cells is below the saturation threshold. Therefore, and following [11,12], we set

$$\frac{1}{\tau^{11}(\boldsymbol{c})} = \frac{1}{\tau_*^{11}} \psi_+(c^0; c_h^0) \psi_-(c^1; c_s^1), \tag{12}$$

where τ_*^{11} is a constant characteristic proliferation time and $\psi_+(x;\theta)$ is the activation rectified linear unit (ReLU) function defined as:

$$\psi_+(x;\theta) = \begin{cases} 0 & \text{if } x < 0, \\ x/\theta & \text{if } 0 \le x \le \theta, \\ 1 & \text{if } x > \theta. \end{cases} \tag{13}$$

For the differentiation process, we model the necrosis and apoptosis phenomena using a two-parameter sigmoid model (see [11,12] for details). Consequently,

$$\frac{1}{\tau^{12}(\boldsymbol{c})} = \frac{1}{\tau_*^{12}}\chi(c^0; c_a^0, \Delta c_a^0), \tag{14}$$

where τ_*^{12} is a constant characteristic death time, c_a^0 is the anoxia death threshold, Δc_a^0 is the anoxia death sensibility and the function χ is defined as:

$$\chi(c^0; c_a^0, \Delta c_a^0) = \frac{1}{2}\left(1 - \tanh\left(\frac{c^0 - c_a^0}{\Delta c_a^0}\right)\right). \tag{15}$$

Here, c_a^0 and Δc_a^0 are the location and spread parameters that characterize the oxygen concentration level that triggers cell death. Sigmoidal activation functions (e.g., logistic or Hill-type laws) are commonly employed in biological modeling to represent S-shaped transition regions (see [37]). The hyperbolic tangent formulation used here is algebraically equivalent to a logistic function and provides a smooth transition between survival and death states. For instance, [38,39] adopt similar hyperbolic-tangent-based formulations to model phenotypic transitions.

To complete the living cell model, suitable boundary conditions are prescribed. Similarly to the oxygen model, homogeneous Neumann boundary conditions are imposed on the solid walls of the central chamber and on the inlet valves, which are assumed to be impermeable to cells. These conditions model zero flux across these boundaries and correspond to $\Gamma_N^1 = \Gamma^{\text{sw}} \cup \Gamma^{\text{in}}$ and $g_N^1 = 0$ in Eq. (6). On the lateral openings, a Robin boundary condition is imposed. This choice is supported by experimental evidence indicating that cell behavior in these regions is influenced by both diffusive processes and environmental factors [11]. Specifically, we set $\Gamma_R^1 = \Gamma^{\text{op}}$, with the values of g_R^1 and γ^1 determined in each experimental setup. Finally, since no Dirichlet boundary conditions are considered for the living cells, we set $\Gamma_D^1 = \emptyset$.

Dead cells. Analogously to the case of living cells, the governing equation for the concentration of dead cells, $c^2(\boldsymbol{x}, t)$, is obtained by particularizing Eqs. (1), (3) and (5) to the current model:

$$\frac{\partial c^2}{\partial t} + \nabla \cdot \boldsymbol{f}^2 = s^2 \quad \text{for} \quad \boldsymbol{f}^2 = -\boldsymbol{A}^2 \nabla c^2 + c^2 \boldsymbol{B}^{20} \nabla c^0 \quad \text{and} \quad s^2 = \frac{1}{\tau^{22}} c^2 - \frac{1}{\tau^{21}} c^2 + \frac{1}{\tau^{12}} c^1.$$

Following [8,11], we assume that dead cells neither interact with the hydrogel mixture nor migrate by diffusion or chemotaxis. Consequently, we set $\boldsymbol{A}^2(\boldsymbol{c}) = \boldsymbol{B}^{20}(\boldsymbol{c}) = \boldsymbol{0}$, which implies $\boldsymbol{f}^2 = 0$. As a result, the transport Eq. (1) reduces to:

$$\frac{\partial c^2}{\partial t} = s^2.$$

Since no spatial derivatives are present, the equation can be solved pointwise in space; that is, for each fixed spatial point $\boldsymbol{x} \in \Omega$, the map $t \mapsto c^2(\boldsymbol{x}, t)$ satisfies an ordinary differential equation in time. Thus, no boundary conditions are required in this case.

To account for the biological behavior of dead cells, the source term is derived by recognizing that dead cells neither proliferate nor revert to a living state. Consequently, the terms containing the characteristic times $\tau^{22}(\boldsymbol{c})$ and $\tau^{21}(\boldsymbol{c})$ are not present in the model, since no such processes occur. As a result, the time evolution of the concentration of dead cells is governed solely by the characteristic time associated with cell death, $\tau^{12}(\boldsymbol{c})$, since the source term reduces to

$$s^2 = \frac{1}{\tau^{12}} c^1, \tag{16}$$

where $\tau^{12}(\boldsymbol{c})$ is defined using Eq. (14).

Table 1 summarizes our specific model, which consists of three coupled nonlinear PDEs. While all three equations are PDEs, the equation governing the dead cells lacks spatial derivatives, making it possible to reduce it to an ODE at each spatial point. The nonlinear coupling in the system arises from the chemotaxis matrix, $\boldsymbol{B}^{10}(c^0, c^1)$ defined in Eq. (9), and the source terms $s^0(c^0, c^1)$, $s^1(c^0, c^1)$, and $s^2(c^0, c^1)$, given in Eqs. (7), (11) and (16). Since the oxygen and living cells equations are independent of the dead cell concentration, these PDEs can be solved as a coupled system. Once the concentrations for the oxygen and living cells are obtained, they can be used to compute the source term in the remaining equation, enabling the determination of the dead cell concentration by solving an ODE for each spatial point.

2.3. Model parameters

The mathematical model introduced in the previous section and summarized in Table 1 is completed by specifying the value of the parameters involved in the model. Refs. [11,12] provide an extensive review of the parameter values reported in the literature, along with a detailed sensitivity analysis that determines the selection of the set of parameters presented in Table 2. The selected

Table 1
3D coupled nonlinear model with two cell phenotypes and one chemical species.

Model	Equations	
Oxygen c^0	$\frac{\partial c^0}{\partial t} - \nabla \cdot (\boldsymbol{A}^0 \nabla c^0) = -\alpha_*^{01} \frac{c^0}{c^0 + c_m^0} c^1$	**COUPLED EQUATIONS**
Living cells c^1	$\frac{\partial c^1}{\partial t} - \nabla \cdot (\boldsymbol{A}^1 \nabla c^1) + \nabla \cdot (\psi_-(c^0; c_h^0)\psi_-(c^1; c_s^1) c^1 \boldsymbol{B}_*^{10} \nabla c^0) = \frac{1}{\tau_*^{11}} \psi_+(c^0; c_h^0)\psi_-(c^1; c_s^1) c^1 - \frac{1}{\tau_*^{12}} \chi(c^0; c_a^0, \Delta c_a^0) c^1$	
Dead cells c^2	$\frac{\partial c^2}{\partial t} = \frac{1}{\tau_*^{12}} \chi(c^0; c_a^0, \Delta c_a^0) c^1$	**ODE for each x**

Table 2
Parameters for the 3D model with two cell phenotypes and one chemical species.

Parameter name	Symbol	Value	Units
Oxygen diffusion	A^0	10^{-3}	mm^2/s
Oxygen consumption rate	α_*^{01}	10^{-6}	mmHg × mm^3/(cell × s)
Saturation Michaelis–Menten const.	c_m^0	2.5	mmHg
Living cell diffusion	A^1	6.6×10^{-8}	mm^2/s
Living cell chemotaxis	B_*^{10}	7.5×10^{-7}	mm^2/(mmHg × s)
Hypoxia migration threshold	c_h^0	7	mmHg
Living cell saturation threshold	c_s^1	5×10^4	cell/mm^3
Characteristic proliferation time	τ_*^{11}	7.2×10^5	s
Death characteristic time	τ_*^{12}	1.728×10^5	s
Anoxia death threshold	c_a^0	1.6	mmHg
Anoxia death sensibility	Δc_a^0	0.1	mmHg

parameters have previously been tested in the corresponding one-dimensional version of the present GBM progression model [11,12] and are adopted here as reference values for the present study.

It is worth noting that in all the examples, the diffusion and chemotaxis matrices are assumed to be isotropic. Specifically, we set $\boldsymbol{A}^0 = A^0\mathbf{I}$, $\boldsymbol{A}^1 = A^1\mathbf{I}$ and $\boldsymbol{B}_*^{10} = B_*^{10}\mathbf{I}$ where $A^0 \in \mathbb{R}$, $A^1 \in \mathbb{R}$, $B_*^{10} \in \mathbb{R}$, and $\mathbf{I}$ denotes the identity matrix. Consequently, Table 2 also lists the corresponding scalar values for the constant parameters A^0, A^1 and B_*^{10}. It is worth noting that while diffusion matrices are homogeneous, according to Eq. (9) the chemotaxis matrix is non-homogeneous.

3. Numerical model

This section presents the numerical approximation of the 3D model involving two cell phenotypes and one chemical species, as introduced in Section 2.2. The strong form of the problem is: find the evolution of the concentrations of oxygen $c^0(\boldsymbol{x}, t)$, living cells $c^1(\boldsymbol{x}, t)$, and dead cells $c^2(\boldsymbol{x}, t)$, verifying the general transport Eq. (1) with the fluxes defined in (2) and (3), and source terms given by (4) and (5).

Assuming a single chemical species ($n_1 = 1$) and two cell phenotypes ($n_2 = 2$), the governing equations take the form:

$$\frac{\partial c^i}{\partial t} + \nabla \cdot (-\boldsymbol{A}^i \nabla c^i + c^i \boldsymbol{B}^{i0} \nabla c^0) = s^i \qquad \text{for } i = 0, 1, 2, \tag{17}$$

where $\boldsymbol{B}^{00} = \mathbf{0}$ and $\boldsymbol{A}^0 = A^0\mathbf{I}$ for oxygen, $\boldsymbol{B}^{10} = \boldsymbol{B}^{10}(c^0, c^1)$ and $\boldsymbol{A}^1 = A^1\mathbf{I}$ for living cells, and $\boldsymbol{A}^2 = \boldsymbol{B}^{20} = \mathbf{0}$ for dead cells. Also, in all three cases $s^i(c^0, c^1)$. Suitable initial and boundary conditions are imposed as described in Eq. (6).

3.1. Weak form in space and functional spaces

To derive the weak variational form of the previous problem, we first introduce the standard Sobolev spaces associated with the Dirichlet boundary Γ_D^i. Specifically, we define the spaces of test functions and admissible functions as follows:

$$V_0^i = \{v \in H^1(\Omega) \ : \ v_{|\Gamma_D^i} = 0\} \qquad \text{and} \qquad V_D^i = \{v \in H^1(\Omega) \ : \ v_{|\Gamma_D^i} = g_D^i\},$$

For the type of problems addressed in this work, we assume that the Dirichlet boundary conditions g_D^i are time-independent (in the microfluidic devices modeled here, oxygen is supplied with a constant concentration value via the lateral channels), and that they are sufficiently smooth to admit a lifting function $c_D^i \in V_D^i$, such that $c_D^i|_{\Gamma_D^i} = g_D^i$. Note that, in this case, any function $v \in V_D^i$ may be rewritten as $v = v_0 + c_D^i$, where $v_0 \in V_0^i$. For Dirichlet data varying in time, the admissible space V_D^i must be defined as a time-dependent space. In the case of dead cells, since no boundary conditions are imposed, $\Gamma_D^2 = \emptyset$, and thus $V_0^2 = V_D^2 = H^1(\Omega)$.

It is also convenient to redefine the concentration $c^i(\boldsymbol{x}, t)$, where $\boldsymbol{x} \in \Omega$ and $t \in I$, as a time-dependent function $c^i(t)$ with values in V_D^i. That is, for each $t \in I$ we have $c^i(t) \in V_D^i$. This can be expressed schematically as:

$$\begin{array}{rccc} c^i : & I & \longrightarrow & V_D^i \\ & t & \longmapsto & c^i(t) \end{array} \qquad \text{and} \qquad \begin{array}{rccc} c^i(t) : & \Omega & \longrightarrow & \mathbb{R} \\ & \boldsymbol{x} & \longmapsto & c^i(t)(\boldsymbol{x}) = c^i(\boldsymbol{x}, t). \end{array} \tag{18}$$

More specifically, the weak solutions c^i belong to the space

$$W^i = \{v \text{ such that } v = c_D^i + v_0, \text{ for } v_0 \in L^2(I; V_0^i) \text{ and } \partial v_0/\partial t \in L^2(I; (V_0^i)')\},$$

where $L^2(I; V_0^i)$ (resp. $L^2(I; (V_0^i)')$) denotes the Bochner space associated to V_0^i of square-integrable functions from I into V_0^i (resp. $(V_0^i)'$). The reader is referred to [40,41] for further details.

In the remainder of the paper, both notations —$c^i(\boldsymbol{x}, t)$ and $c^i(t)$— are used interchangeably for concentrations and other functions, depending on the context for simplicity of notation.

The weak form (integrated in space) of (17) for oxygen and living cells ($i = 0, 1$) reads: find $c^i(t) \in V_D^i$ that satisfies the initial condition $c^i(0) = c^{i,0}$ such that, for almost every $t \in (0, T)$,

$$\begin{aligned}\int_\Omega \frac{\partial c^i}{\partial t} v^i \,\mathrm{d}\Omega + \int_\Omega A^i \boldsymbol{\nabla} c^i \cdot \boldsymbol{\nabla} v^i \,\mathrm{d}\Omega - \int_\Omega c^i \boldsymbol{B}^{i0}(c^0, c^1) \boldsymbol{\nabla} c^0 \cdot \boldsymbol{\nabla} v^i \,\mathrm{d}\Omega + \int_{\Gamma_R^i} \gamma^i c^i v^i \,\mathrm{d}\Gamma \\ = \int_\Omega s^i(c^0, c^1) v^i \,\mathrm{d}\Omega - \int_{\Gamma_N^i} g_N^i v^i \,\mathrm{d}\Gamma + \int_{\Gamma_R^i} \gamma^i g_R^i v^i \,\mathrm{d}\Gamma,\end{aligned} \tag{19}$$

for all $v^i \in V_0^i$. This weak form is obtained by multiplying Eq. (17) by a test function, $v^i \in V_0^i$, integrating over the spatial domain Ω, applying the divergence theorem, and incorporating the boundary conditions defined in Eq. (6). Note that A^i, γ^i, g_N^i and g_R^i are real constants, and we assume that for a.e. $t \in I$, $s^i(c^0, c^1) \in L^2(\Omega)$ and $\boldsymbol{B}^{i0}(c^0, c^1) \in [L^\infty(\Omega)]^d$.

3.2. Space discretization

We discretize the domain of the microfluidic device, Ω, using a tessellation $\mathcal{T}_h$ composed of non-overlaping and non-degenerate elements K that partition Ω. This tessellation is used to define the finite-dimensional continuous spaces V_{h0}^i and V_{hD}^i, of associated polynomial degree p. Specifically, let $\boldsymbol{x}_j$, $j = 1, \dots, n_{\text{np}}$, denote the mesh nodes of the computational mesh $\mathcal{T}_h$, where n_{np} is the total number of nodes. Also, let N_j be the corresponding continuous Lagrange basis functions, such that $N_j(\boldsymbol{x}_i) = \delta_{ij}$. Finally, define $\mathcal{D}^i$ as the set of indices of the nodes lying on the Dirichlet boundary Γ_D^i, that is, $j \in \mathcal{D}^i$ implies $\boldsymbol{x}_j \in \Gamma_D^i$, and let $\mathcal{N}^i = \{1, \dots, n_{\text{np}}\} \backslash \mathcal{D}^i$ be its complementary set (nodes where the solution is unknown).

The discrete test and admissible functions spaces are then given by

$$V_{h0}^i = \{v \ : \ v = \sum_{j \in \mathcal{N}^i} v_j N_j(\boldsymbol{x}),\ v_j \in \mathbb{R}\}$$

and

$$V_{hD}^i = \{v \ : \ v = \sum_{j \in \mathcal{N}^i} v_j N_j(\boldsymbol{x}) + \sum_{j \in \mathcal{D}^i} g_D^i(\boldsymbol{x}_j) N_j(\boldsymbol{x}),\ v_j \in \mathbb{R}\}.$$

With these notations, the discrete-in-space approximations of oxygen, living cell, and dead cell concentrations are written as:

$$c_h^i(\boldsymbol{x}, t) = \sum_{j=1}^{n_{\text{np}}} N_j(\boldsymbol{x}) c_{hj}^i(t) = \sum_{j \in \mathcal{N}^i} N_j(\boldsymbol{x}) c_{hj}^i(t) + \sum_{j \in \mathcal{D}^i} N_j(\boldsymbol{x}) c_{hj}^i(t) \qquad \text{for } i = 0, 1, 2, \tag{20}$$

where $c_{hj}^i = c_h^i(\boldsymbol{x}_j, t)$ for $j \in \mathcal{N}^i$, and $c_{hj}^i(t) = g_D^i(\boldsymbol{x}_j)$ for $j \in \mathcal{D}^i$, since the concentration values at Dirichlet nodes are prescribed by constant boundary conditions. Note that, as stated in Section 3.1, the Dirichlet data g_D^i are assumed to be time-independent. The corresponding time derivatives are given by

$$\frac{\partial c_h^i}{\partial t} = \sum_{j \in \mathcal{D}^i} N_j(\boldsymbol{x}) \dot{c}_{hj}^i(t) + \sum_{j \in \mathcal{N}^i} N_j(\boldsymbol{x}) \dot{c}_{hj}^i(t) = \sum_{j \in \mathcal{N}^i} N_j(\boldsymbol{x}) \dot{c}_{hj}^i(t) \qquad \text{for } i = 0, 1, 2, \tag{21}$$

where the simplification follows from the fact that $c_{hj}^i(t) = g_D^i(\boldsymbol{x}_j)$ is constant in time for $j \in \mathcal{D}^i$, and hence $\dot{c}_{hj}^i(t) = 0$ on $\mathcal{D}^i$.

Finally, we introduce the vectors containing the unknown nodal values of the concentrations and their time derivatives, denoted by $\boldsymbol{c}_h^i(t)$ and $\dot{\boldsymbol{c}}_h^i(t)$, respectively. Specifically, $\boldsymbol{c}_h^i(t)$ and $\dot{\boldsymbol{c}}_h^i(t)$ contain the time-dependent values $c_{hj}^i(t) \in [L^2([0, T])]^{n_{\text{np}}^i}$ and $\dot{c}_{hj}^i(t) \in [L^2([0, T])]^{n_{\text{np}}^i}$ for all $j \in \mathcal{N}^i$, where $n_{\text{np}}^i = n(\mathcal{N}^i)$ is the number of mesh nodes in $\mathcal{N}^i$. That is,

$$\boldsymbol{c}_h^i(t) = [c_{hj}^i(t)]_{j \in \mathcal{N}^i} \quad \text{and} \quad \dot{\boldsymbol{c}}_h^i(t) = [\dot{c}_{hj}^i(t)]_{j \in \mathcal{N}^i}. \tag{22}$$

In the remainder of the paper, the explicit dependence with respect to time may be omitted for clarity of presentation.

The semi-discrete approximations of the oxygen and living cell concentrations, $c_h^0(t) \in V_{hD}^0$ and $c_h^1(t) \in V_{hD}^1$ respectively, are obtained by solving the following semi-discrete problem: find $c_{hj}^0(t) \in L^2([0, T])$ for $j \in \mathcal{N}^0$, and $c_{hj}^1(t) \in L^2([0, T])$ for $j \in \mathcal{N}^1$ such

Table 3
Butcher table for a diagonal implicit Runge–Kutta scheme.

c_1	a_{11}			
c_2	a_{21}	a_{22}		
$\vdots$	$\vdots$	$\vdots$	$\ddots$	
c_s	a_{s1}	a_{s2}	$\cdots$	a_{ss}
	b_1	b_2	$\cdots$	b_s

that for all $t \in [0,T]$

$$
\begin{aligned}
R^0_\alpha &= \sum_{j=1}^{n_{\text{np}}} \dot{c}^0_{hj} \int_\Omega N_j N_\alpha \,\mathrm{d}\Omega + \sum_{j=1}^{n_{\text{np}}} c^0_{hj} \int_\Omega \boldsymbol{A}^0 \boldsymbol{\nabla} N_j \cdot \boldsymbol{\nabla} N_\alpha \,\mathrm{d}\Omega + \sum_{j=1}^{n_{\text{np}}} c^0_{hj} \int_{\Gamma^0_R} \gamma^0 N_j N_\alpha \,\mathrm{d}\Gamma \\
&\quad - \int_\Omega s^0(c^0_h, c^1_h) N_\alpha \,\mathrm{d}\Omega + \int_{\Gamma^0_N} g^0_N N_\alpha \,\mathrm{d}\Gamma - \int_{\Gamma^0_R} \gamma^0 g^0_R N_\alpha \,\mathrm{d}\Gamma = 0 \qquad \text{for } \alpha \in \mathcal{N}^0, \\
R^1_\alpha &= \sum_{j=1}^{n_{\text{np}}} \dot{c}^1_{hj} \int_\Omega N_j N_\alpha \,\mathrm{d}\Omega + \sum_{j=1}^{n_{\text{np}}} c^1_{hj} \int_\Omega \boldsymbol{A}^1 \boldsymbol{\nabla} N_j \cdot \boldsymbol{\nabla} N_\alpha \,\mathrm{d}\Omega \\
&\quad - \sum_{r=1}^{n_{\text{np}}} \sum_{j=1}^{n_{\text{np}}} c^1_{hj} c^0_{hr} \int_\Omega N_j \boldsymbol{B}^{10}(c^0_h, c^1_h) \boldsymbol{\nabla} N_r \cdot \boldsymbol{\nabla} N_\alpha \,\mathrm{d}\Omega + \sum_{j=1}^{n_{\text{np}}} c^1_{hj} \int_{\Gamma^1_R} \gamma^1 N_j N_\alpha \,\mathrm{d}\Gamma \\
&\quad - \int_\Omega s^1(c^0_h, c^1_h) N_\alpha \,\mathrm{d}\Omega + \int_{\Gamma^1_N} g^1_N N_\alpha \,\mathrm{d}\Gamma - \int_{\Gamma^1_R} \gamma^1 g^1_R N_\alpha \,\mathrm{d}\Gamma = 0 \qquad \text{for } \alpha \in \mathcal{N}^1.
\end{aligned}
\tag{23}
$$

For clarity of presentation, the semi-discrete approximations c^0_h and c^1_h from Eq. (20) are not explicitly substituted in the nonlinear terms $s^1(c^0_h, c^0_h)$, $\boldsymbol{B}^{10}(c^0_h, c^1_h)$ and $s^1(c^0_h, c^1_h)$. Also recall that for $j \in \mathcal{D}^0$, $c^0_{hj}(t) = g^0_D(\boldsymbol{x}_j)$ and analogously for $j \in \mathcal{D}^1$, $c^1_{hj}(t) = g^1_D(\boldsymbol{x}_j)$.

These equations are derived from the weak form (19) by substituting the semi-discrete approximations $c^i = c^0_h$ and $c^i = c^1_h$ from Eq. (20), and using $v^i = N_\alpha$ as a test function. It is worth noting that the resulting semi-discrete system for oxygen and living cells forms a coupled system of nonlinear ODEs.

The semi-discrete approximation of the dead cell concentration, $c^2_h(t) \in V^0_{hD}$, is obtained by solving the following uncoupled system of ODEs: find $c^2_{hj}(t) \in L^2([0,T])$ such that

$$
R^2_j = \dot{c}^2_{hj} - s^2(c^0_{hj}(t), c^1_{hj}(t)) = 0 \qquad \text{for } j = 1, \dots, n_{\text{np}}. \tag{24}
$$

These equations are obtained by directly enforcing the governing Eq. (17) at each mesh node $\boldsymbol{x} = \boldsymbol{x}_j$, noting that for dead cells $\boldsymbol{A}^2 = \boldsymbol{B}^{20} = \boldsymbol{0}$. Note that the uncoupled system of ODEs (24) can be solved once the solution of the coupled system (23) is known at all mesh nodes.

Finally, introducing the vectors of residuals $\boldsymbol{R}^0 = [R^0_\alpha]_{\alpha \in \mathcal{N}^0}$, $\boldsymbol{R}^1 = [R^1_\alpha]_{\alpha \in \mathcal{N}^1}$, and $\boldsymbol{R}^2 = [R^2_\alpha]_{\alpha = 1, \dots, n_{\text{np}}}$, and using the corresponding vectors of unknown concentrations and their time derivatives at the mesh nodes defined in Eq. (22), the semi-discrete problem for the GBM progression can be stated as follows. First, find $\boldsymbol{c}^0_h(t) \in [L^2([0,T])]^{n^0_{\text{np}}}$ and $\boldsymbol{c}^1_h(t) \in [L^2([0,T])]^{n^1_{\text{np}}}$ by solving the coupled system of nonlinear first-order ordinary differential equations:

$$
\boldsymbol{R}^{01}(t, \dot{\boldsymbol{c}}^0_h, \boldsymbol{c}^0_h, \dot{\boldsymbol{c}}^1_h, \boldsymbol{c}^1_h) = \begin{bmatrix} \boldsymbol{R}^0(t, \dot{\boldsymbol{c}}^0_h, \boldsymbol{c}^0_h, \boldsymbol{c}^1_h) \\ \boldsymbol{R}^1(t, \dot{\boldsymbol{c}}^1_h, \boldsymbol{c}^0_h, \boldsymbol{c}^1_h) \end{bmatrix} = \boldsymbol{0}, \tag{25}
$$

and then, find $\boldsymbol{c}^2_h(t) \in [L^2([0,T])]^{n_{\text{np}}}$ solving the uncoupled system of first-order ordinary differential equations:

$$
\boldsymbol{R}^2(t, \dot{\boldsymbol{c}}^2_h, \boldsymbol{c}^0_h, \boldsymbol{c}^1_h) = \boldsymbol{0}. \tag{26}
$$

3.3. Time discretization

To solve the system of ODEs (25) and (26), we employ a Diagonally Implicit Runge–Kutta (DIRK) method. These methods are schematically represented by the Butcher table (see Table 3) where s is the number of stages of the method, c_k for $k = 1, \dots, s$ are the abscissa, b_k for $k = 1, \dots, s$ are the weights, and a_{lk} for $l = 1, \dots, s$ and $k = 1, \dots, l$ are the internal coefficients. For further details on DIRK methods and their associated Butcher table, the reader is referred to [16–19].

Let $0 = t_0 < t_1 < \cdots < t_n < t_{n+1} < \cdots < t_N = T$ be a partition of the time interval into N time slabs $I_n = [t^n, t^{n+1}]$, each of length $\Delta t_n = t_{n+1} - t_n$, for $n = 0, \dots, N-1$. For simplicity of presentation, we assume a constant time increment $\Delta t_n = \Delta t = T/N$. Within each time slab I_n, we define the intermediate times (or stages) of the DIRK method as $t^{n,l} = t^n + c_l \Delta t$, for $l = 1, \dots, s$, where the coefficients c_l are the abscissae of the method (see Fig. 3).

We denote by $(\cdot)^n$ the value of any time-dependent quantity at time t^n, and by $(\cdot)^{n,l}$ its value at the intermediate time $t^{n,l}$. Given a time slab $I_n = [t^n, t^{n+1}]$ and the known concentration $\boldsymbol{c}^{i,n}_h = \boldsymbol{c}^i_h(t^n)$ at the initial time of the slab, the DIRK method computes the

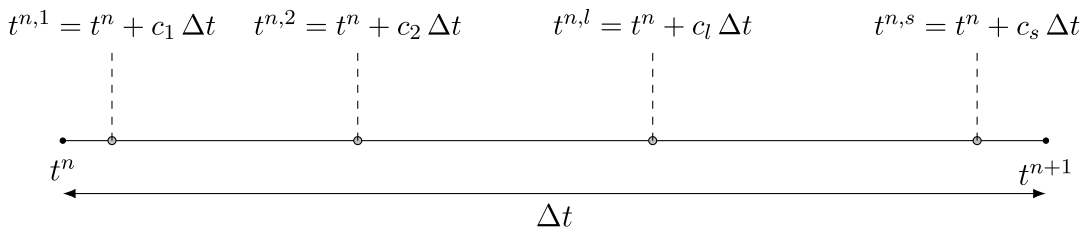

Fig. 3. Illustration of the DIRK time steps inside the slab $I_n = [t^n, t^{n+1}]$. Each intermediate time $t^{n,l} = t^n + c_l \Delta t$ corresponds to an implicit stage in the Runge–Kutta scheme.

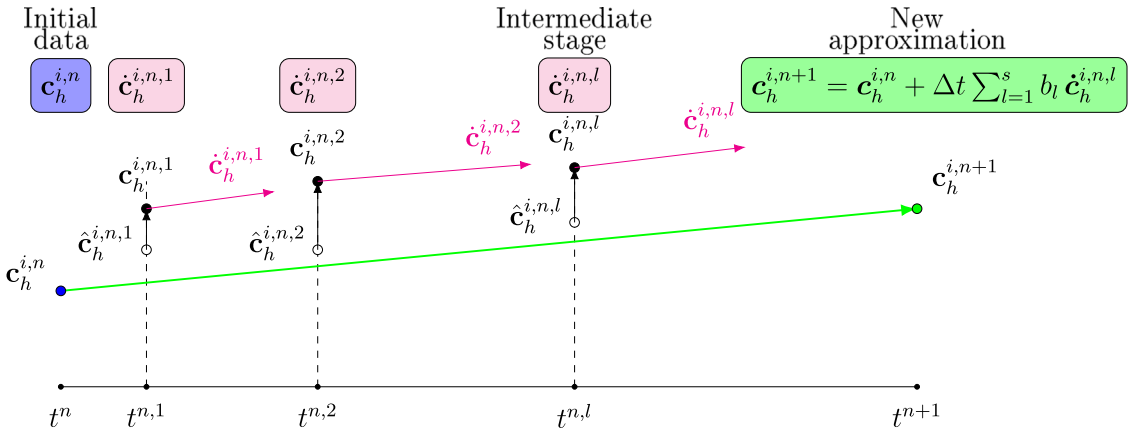

Fig. 4. Illustration of the DIRK approximation. At each time slab $I_n = [t^n, t^{n+1}]$, the new approximation $\mathbf{c}^{i,n+1}$ is computed from the initial data $\mathbf{c}^{i,n}$ by computing the derivatives $\dot{\mathbf{c}}^{i,n,l}$ at s intermediate stages. At each stage, the explicit part $\hat{\mathbf{c}}^{i,n,l}$ is first computed. Then, $\mathbf{c}^{i,n,l}$ is found solving the appropriate residual equation. Finally, $\dot{\mathbf{c}}^{i,n,l}$ is recovered from $\hat{\mathbf{c}}^{i,n,l}$ and $\mathbf{c}^{i,n,l}$.

concentration at the next time step t^{n+1}, namely $c_h^{i,n+1} = c_h^i(t^{n+1})$ as follows:

$$c_h^{i,n+1} = c_h^{i,n} + \Delta t \sum_{l=1}^{s} b_l\, \dot{c}_h^{i,n,l} \tag{27}$$

where b_l is the l-th weight, $\dot{c}_h^{i,n,l}$ is the approximation of $\dot{c}_h^i$ at the intermediate time $t^{n,l}$, that is, $\dot{c}_h^{i,n,l} \approx \dot{c}_h^i(t^{n,l})$, as illustrated in Fig. 4.

To compute the intermediate stage derivatives $\dot{c}_h^{i,n,l}$ at time $t^{n,l}$, an implicit scheme is employed that involves both the stage derivatives $\dot{c}_h^{i,n,l}$ and the corresponding concentration approximations $c_h^{i,n,l} \approx c_h^i(t^{n,l})$. Specifically, the concentration at each stage $l = 1, \ldots, s$ is given by:

$$c_h^{i,n,l} = c_h^{i,n} + \Delta t \sum_{k=1}^{l} a_{lk}\, \dot{c}_h^{i,n,k} = \hat{c}_h^{i,n,l} + \Delta t\, a_{ll}\, \dot{c}_h^{i,n,l}, \tag{28}$$

where the predictor (explicit part) is defined as:

$$\hat{c}_h^{i,n,l} = c_h^{i,n} + \Delta t \sum_{k=1}^{l-1} a_{lk}\, \dot{c}_h^{i,n,k}.$$

Note that, in the computation of the intermediate concentration $c^{i,n,l}$ at stage l, the term $\hat{c}^{i,n,l}$ is already known, since it only involves the concentration at the previous time step and the time derivatives from earlier stages $k < l$. Thus, the only unknowns at each stage are the concentration $c_h^{i,n,l}$ and the time derivative $\dot{c}_h^{i,n,l}$.

In this work, rather than solving directly for the intermediate stage time derivatives, $\dot{c}_h^{i,n,l}$, we reformulate the problem by treating the concentrations $c_h^{i,n,l}$ as the primary unknowns. To this end, we replace the stage time derivative in the residual Eqs. (25) and (26) with its equivalent expression from Eq. (28):

$$\dot{c}_h^{i,n,l} = \frac{c_h^{i,n,l} - \hat{c}_h^{i,n,l}}{\Delta t\, a_{ll}}. \tag{29}$$

This substitution allows the stage residuals to be expressed solely in terms of the concentration variables $c_h^{i,n,l}$, which are then the only unknowns to be determined at each stage of the DIRK method.

Specifically, at each stage $l = 1, \dots, s$, we first solve the following nonlinear coupled system to determine $\boldsymbol{c}_h^{0,n,l}$ and $\boldsymbol{c}_h^{1,n,l}$:

$$\boldsymbol{R}\left(\boldsymbol{c}_h^{0,n,l}, \boldsymbol{c}_h^{1,n,l}\right) = \boldsymbol{R}^{01}\left(t^{n,l}, \frac{\boldsymbol{c}_h^{0,n,l} - \hat{\boldsymbol{c}}_h^{0,n,l}}{\Delta t\, a_{ll}}, \boldsymbol{c}_h^{0,n,l}, \frac{\boldsymbol{c}_h^{1,n,l} - \hat{\boldsymbol{c}}_h^{1,n,l}}{\Delta t\, a_{ll}}, \boldsymbol{c}_h^{1,n,l}\right) = \boldsymbol{0}. \tag{30}$$

Then, the corresponding stage derivatives $\dot{\boldsymbol{c}}_h^{0,n,l}$ and $\dot{\boldsymbol{c}}_h^{1,n,l}$ are recovered using Eq. (29).

Once the concentrations of oxygen and living cells are known for the current stage, the concentration of dead cells, $\boldsymbol{c}_h^{2,n,l}$, is computed solving the following uncoupled linear system:

$$\boldsymbol{R}^2\left(t^{n,l}, \frac{\boldsymbol{c}_h^{2,n,l} - \hat{\boldsymbol{c}}_h^{2,n,l}}{\Delta t\, a_{ll}}, \boldsymbol{c}_h^{0,n,l}, \boldsymbol{c}_h^{1,n,l}\right) = \boldsymbol{0}. \tag{31}$$

It is worth noting that, due to the specific form of the residual $\boldsymbol{R}^2$ associated with dead cells (whose components are defined in Eq. (24)), the required stage derivatives $\dot{\boldsymbol{c}}_h^{2,n,l}$ can in fact be computed directly by evaluating the source term $s^2(\boldsymbol{c}_h^{0,n,l}, \boldsymbol{c}_h^{1,n,l})$ using the current-stage concentrations. That is,

$$\dot{\boldsymbol{c}}_h^{2,n,l} = s^2(\boldsymbol{c}_h^{0,n,l}, \boldsymbol{c}_h^{1,n,l}).$$

Finally, once all stages are completed, the concentrations at the next time step, $\boldsymbol{c}_h^{0,n+1}$, $\boldsymbol{c}_h^{1,n+1}$, and $\boldsymbol{c}_h^{2,n+1}$, are computed using Eq. (27).

The detailed formulas for the residuals defined in Eqs. (30) and (31) are provided in Appendix A.

3.4. Nonlinear solver: the FE-DIRK-Newton formulation

The FE-DIRK discretization of Eq. (17) consists in finding the time and space-discrete concentration field

$$c^i_{h,\Delta t}(\boldsymbol{x}, t) = \sum_{n=0}^{N} \sum_{j=1}^{n_{\text{np}}} N_j(\boldsymbol{x}) N_n^{\Delta}(t) c_{hj}^{i,n} \qquad \text{for } i = 0, 1, 2, \tag{32}$$

where $\{N_n^{\Delta}\}_{n=0,\dots,N}$ are the linear basis functions associated with the time discretization. Analogously to Eq. (22), the vector $\boldsymbol{c}_h^{i,n}$ contains the nodal unknowns of the concentration $c_h^i(\boldsymbol{x}, t^n)$, evaluated at the mesh nodes $\boldsymbol{x}_j$, for $j \in \mathcal{N}^i$:

$$\boldsymbol{c}_h^{i,n} = [c_{hj}^{i,n}]_{j \in \mathcal{N}^i} \quad \text{where} \quad c_{hj}^{i,n} \approx c_{hj}^i(t^n) = c_h^i(\boldsymbol{x}_j, t^n).$$

It is worth noting that the time shape functions $N_n^{\Delta}(t)$ are introduced solely to reconstruct a continuous-in-time solution from the discrete DIRK stage values for post-processing purposes. They are not involved in the numerical time integration performed by the DIRK scheme itself. Since DIRK methods compute multiple internal stage solutions within each time step (beyond the initial and final points), these intermediate values can be used to construct more accurate time-continuous reconstructions. Specifically, continuous extensions — also known as dense output formulas — have been developed for high-order DIRK schemes (see for instance [42,43]). In this context, a continuous-in-time extension of Eq. (27) can be written as:

$$c^i_{h,\Delta t}(\boldsymbol{x}, t^n + \theta \Delta t) = \sum_{j=1}^{n_{\text{np}}} N_j(\boldsymbol{x}) c_{hj}^{i,n} + \Delta t \sum_{l=1}^{s} \sum_{j=1}^{n_{\text{np}}} N_j(\boldsymbol{x}) b_l(\theta) \dot{c}_{hj,l}^{i,n} \qquad \text{for } i = 0, 1, 2. \tag{33}$$

where $\theta \in [0, 1)$ and $n = 0, \dots, N-1$. The time-dependent interpolation coefficients $b_l(\theta)$ are chosen to match the order of accuracy of the DIRK scheme and provide a dense output over each time interval. In this work, however, we restrict ourselves to a simple linear interpolation, as our primary goal is to accurately compute the concentrations at the discrete, predefined times t^n.

The FE-DIRK coefficients at the Dirichlet boundaries are such that $c_{hj}^{i,n} = g_D^i(\boldsymbol{x}_j)$ for all $j \in D^i$ and $n = 0, \dots, N$. For free nodes $j \in \mathcal{N}^i$, the unknowns $c_{hj}^{i,n}$ (stored in $\boldsymbol{c}_h^{i,n}$) are computed using the DIRK time-stepping formula given in Eq. (27). Specifically, to compute the solution at time t^{n+1}, the s intermediate stage approximations $\boldsymbol{c}_h^{i,n,l}$ for $l = 1, \dots, s$ are introduced and computed from the residual Eqs. (30) and (31).

As discussed in the previous section, the concentrations $\boldsymbol{c}_h^{2,n,l}$ for dead cells are computed explicitly once the oxygen and living cell concentrations $\boldsymbol{c}_h^{0,n,l}$ and $\boldsymbol{c}_h^{1,n,l}$ are available. Specifically

$$\boldsymbol{c}_h^{2,n+1} = \boldsymbol{c}_h^{2,n} + \Delta t \sum_{l=1}^{s} b_l\, s^2(\boldsymbol{c}_h^{0,n,l}, \boldsymbol{c}_h^{0,n,l}).$$

The oxygen and living cell concentrations, $\boldsymbol{c}_h^{0,n,l}$ and $\boldsymbol{c}_h^{1,n,l}$, are obtained by solving the nonlinear system defined in Eq. (30), which can be rewritten using the stage residual vectors $\boldsymbol{R}^{0,n,l}$ and $\boldsymbol{R}^{1,n,l}$:

$$\boldsymbol{R}\left(\boldsymbol{c}_h^{0,n,l}, \boldsymbol{c}_h^{1,n,l}\right) = \begin{bmatrix} \boldsymbol{R}^{0,n,l}\left(\boldsymbol{c}_h^{0,n,l}, \boldsymbol{c}_h^{1,n,l}\right) \\ \boldsymbol{R}^{1,n,l}\left(\boldsymbol{c}_h^{0,n,l}, \boldsymbol{c}_h^{1,n,l}\right) \end{bmatrix} = \begin{bmatrix} \boldsymbol{R}^0\left(t^{n,l}, \frac{\boldsymbol{c}_h^{0,n,l} - \hat{\boldsymbol{c}}_h^{0,n,l}}{\Delta t\, a_{ll}}, \boldsymbol{c}_h^{0,n,l}, \boldsymbol{c}_h^{1,n,l}\right) \\ \boldsymbol{R}^1\left(t^{n,l}, \frac{\boldsymbol{c}_h^{1,n,l} - \hat{\boldsymbol{c}}_h^{1,n,l}}{\Delta t\, a_{ll}}, \boldsymbol{c}_h^{0,n,l}, \boldsymbol{c}_h^{1,n,l}\right) \end{bmatrix}. \tag{34}$$

The nonlinear system (34) is solved using Newton's method. That is, for each Newton iteration ν, we update the concentration vectors as

$$\boldsymbol{c}_{h,\nu+1}^{i,n,l} = \boldsymbol{c}_{h,\nu}^{i,n,l} + \delta\boldsymbol{c}_{h,\nu}^{i,n,l} \qquad \text{for } i = 0, 1,$$

where we compute $\delta\boldsymbol{c}_{h,\nu}^{i,n,l}$ by solving the following linear system

$$\begin{bmatrix} \partial_0 \boldsymbol{R}^{0,n,l}\left(\boldsymbol{c}_{h,\nu}^{0,n,l}, \boldsymbol{c}_{h,\nu}^{1,n,l}\right) & \partial_1 \boldsymbol{R}^{0,n,l}\left(\boldsymbol{c}_{h,\nu}^{0,n,l}, \boldsymbol{c}_{h,\nu}^{1,n,l}\right) \\ \partial_0 \boldsymbol{R}^{1,n,l}\left(\boldsymbol{c}_{h,\nu}^{0,n,l}, \boldsymbol{c}_{h,\nu}^{1,n,l}\right) & \partial_1 \boldsymbol{R}^{1,n,l}\left(\boldsymbol{c}_{h,\nu}^{0,n,l}, \boldsymbol{c}_{h,\nu}^{1,n,l}\right) \end{bmatrix} \begin{bmatrix} \delta\boldsymbol{c}_{h,\nu}^{0,n,l} \\ \delta\boldsymbol{c}_{h,\nu}^{1,n,l} \end{bmatrix} = - \begin{bmatrix} \boldsymbol{R}^{0,n,l}\left(\boldsymbol{c}_{h,\nu}^{0,n,l}, \boldsymbol{c}_{h,\nu}^{1,n,l}\right) \\ \boldsymbol{R}^{1,n,l}\left(\boldsymbol{c}_{h,\nu}^{0,n,l}, \boldsymbol{c}_{h,\nu}^{1,n,l}\right) \end{bmatrix}. \tag{35}$$

Here $\partial_j \boldsymbol{R}^{i,n,l}$ denotes the Jacobian matrix containing the partial derivatives of $\boldsymbol{R}^{i,n,l}$ with respect to $\boldsymbol{c}_h^{j,n,l}$, that is

$$\partial_j \boldsymbol{R}^{i,n,l} = \frac{\partial \boldsymbol{R}^{i,n,l}}{\partial \boldsymbol{c}_h^{j,n,l}} \qquad \text{for } i, j = 0, 1. \tag{36}$$

Note that the Jacobian blocks $\partial_0 \boldsymbol{R}^{0,n,l}$ and $\partial_1 \boldsymbol{R}^{1,n,l}$ are square matrices, while the off-diagonal blocks $\partial_0 \boldsymbol{R}^{1,n,l}$ and $\partial_1 \boldsymbol{R}^{0,n,l}$ may be rectangular. Detailed expressions for these Jacobian matrices are provided in Appendix A.

The iterative procedure is terminated when both the relative change between successive iterates falls below a prescribed tolerance ε_c, and the norm of the residual is smaller than a threshold ε_R. These conditions are expressed as

$$\frac{\|\boldsymbol{c}_{h,\nu+1}^{n,l} - \boldsymbol{c}_{h,\nu}^{n,l}\|_2}{\|\boldsymbol{c}_{h,\nu}^{n,l}\|_2} < \varepsilon_c \qquad \text{and} \qquad \|\boldsymbol{R}\left(\boldsymbol{c}_{h,\nu}^{0,n,l}, \boldsymbol{c}_{h,\nu}^{1,n,l}\right)\|_2 < \varepsilon_R,$$

where $\|\cdot\|_2$ denotes the discrete (Euclidean) norm, and $\boldsymbol{c}_{h,\nu}^{n,l} \in \mathbb{R}^{n_{\text{np}}^0 + n_{\text{np}}^1}$ is the concentration vector at iteration ν obtained by staking $\boldsymbol{c}_{h,\nu}^{0,n,l} \in \mathbb{R}^{n_{\text{np}}^0}$ and $\boldsymbol{c}_{h,\nu}^{1,n,l} \in \mathbb{R}^{n_{\text{np}}^1}$.

4. Examples

In this section, we present three numerical examples that illustrate the performance of the FE-DIRK-Newton method introduced above. The first example verifies the convergence properties of the method for different polynomial degrees using a manufactured solution. Examples 2 and 3 reproduce experimental configurations previously reported in the literature [11], where the underlying one-dimensional model was validated against experimental data. These examples are used here to evaluate the accuracy and robustness of the proposed numerical methodology in higher-dimensional settings, rather than to introduce new experimental validation. Specifically, the second example examines the ability of the method to reproduce solutions with a one-dimensional character, as reported in previous studies on GBM progression. This test confirms that our formulation can replicate established results in simplified geometries. The third example involves a fully three-dimensional simulation. In addition to demonstrating the applicability of the method to complex geometries and its ability to resolve spatial features, this example also highlights dynamical characteristics that cannot be observed in purely one- or two-dimensional settings. Specifically, we investigate the formation of necrotic cores and living cell palisades, thereby exploring a range of biologically relevant scenarios.

4.1. Example 1: Convergence analysis with a manufactured solution

This example is designed to validate the convergence properties of the proposed FE-DIRK-Newton method for solving the nonlinear coupled transport problem introduced in Eq. (1). Specifically, we consider the simplified case that involves a single chemical species, oxygen (c^0), and a single cell phenotype, living cells (c^1).

To this end, we define a two-dimensional synthetic problem over the square domain $\Omega = [0, 10] \times [0, 10]$ mm, characterized by a one-dimensional spatial profile, associated with the manufactured solutions:

$$c^0(x, y, t) = 1 + \mathrm{e}^{-t}\cos(\pi x) \quad \text{and} \quad c^1(x, y, t) = 1 + \mathrm{e}^{-t}\sin(\pi x). \tag{37}$$

Dirichlet boundary conditions are imposed on $\partial\Omega$. The prescribed values, as well as the initial condition, are obtained by evaluating the solutions (37).

The governing equations of the problem are obtained from Eqs. (2) and (3) assuming that the diffusion matrices are isotropic and homogeneous, see the end of Section 2.3, and that the chemotaxis matrix is isotropic but varying in space, that is $\boldsymbol{B}^{10} = B^{10}\mathbf{I}$, where $B^{10} = B_*^{10}\,\psi_-(c^0; c_h^0)\,\psi_-(c^1; c_s^1)$. All coefficients ($A^0$, A^1, B_*^{10}, c_h^0, c_s^1) are taken from Table 2.

With these definitions, the equations governing the problem are:

$$\begin{aligned} &\frac{\partial c^0}{\partial t} - \boldsymbol{\nabla}\cdot(A^0\boldsymbol{\nabla}c^0) = s^0, \\ &\frac{\partial c^1}{\partial t} + \boldsymbol{\nabla}\cdot(-A^1\boldsymbol{\nabla}c^1 + c^1 B^{10}\boldsymbol{\nabla}c^0) = s^1. \end{aligned} \tag{38}$$

The source terms s^0 and s^1 are chosen so that the manufactured solutions in Eq. (37) satisfy the governing Eq. (38) exactly. Substituting (37) into Eq. (38), and after some manipulations, yields

$$s^0 = (c^0 - 1)(\pi^2 A^0 - 1),$$

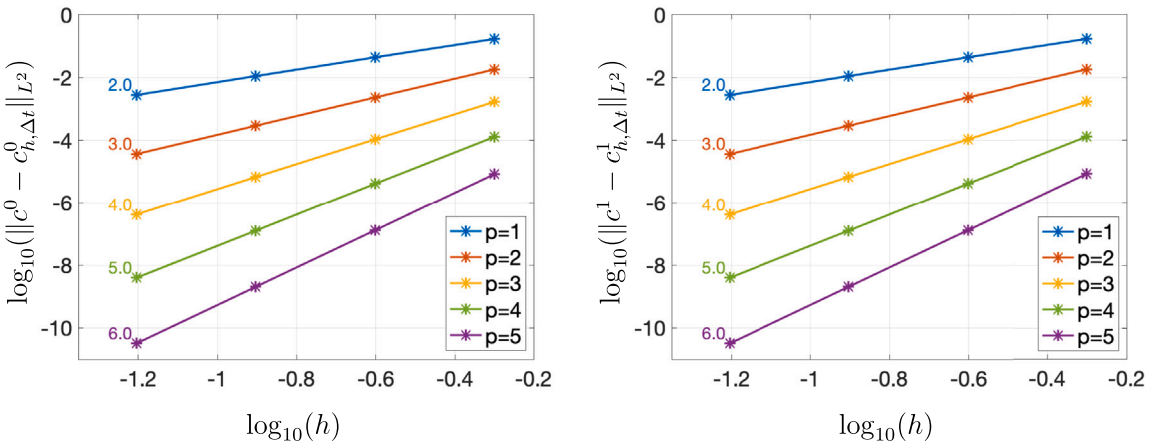

Fig. 5. Convergence plot of the L^2-norm errors, $\|c^i(x, y, 0.002) - c^i_{h,\Delta t}(x, y, 0.002)\|_{L^2(\Omega)}, i = 0, 1$, for oxygen (left) and living cells (right) for the interpolation degrees $p = 1, 2, 3, 4, 5$.

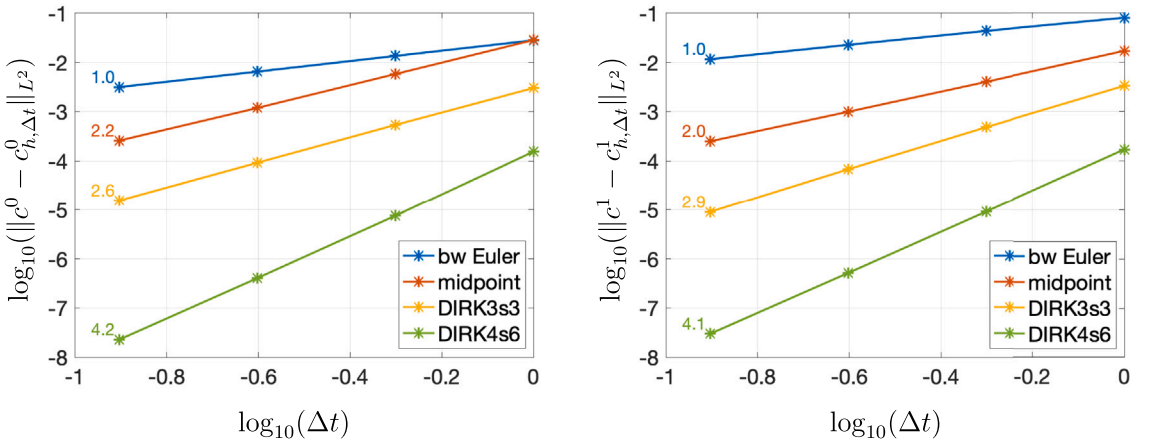

Fig. 6. Convergence plot of the L^2-norm errors, $\|c^i(x, y, 2) - c^i_{h,\Delta t}(x, y, 2)\|_{L^2(\Omega)}, i = 0, 1$, for oxygen (left) and living cells (right) for the four different time-integration schemes (backward Euler, midpoint rule, third order 3 stage DIRK and fourth order DIRK method).

$$s^1 = (c^1 - 1)(\pi^2 A^1 - 1) + \pi^2 B^{10}(1 - c^0)(2c^1 - 1) + \pi c^1(1 - c^1)\frac{\partial B^{10}}{\partial x}.$$

To study the convergence with respect to the spatial discretization, we consider the fixed time interval $I = [0, 0.002]$ hours, and a temporal discretization based on a three-stage DIRK scheme with constant time step $\Delta t = 10^{-4}$ hours, resulting in 20 total time steps. For the spatial discretization we use uniform structured quadrilateral meshes with increasing resolutions of $n = 2, 4, 8, 16$ elements per side (corresponding to element sizes $h = 2^{-1}, 2^{-2}, 2^{-3}, 2^{-4}$) and polynomial degrees $p = 1, 2, 3, 4, 5$.

Fig. 5 shows the L^2-norm errors of the computed solutions at the final simulation time $t = 0.002$ hours, given by

$$\|c^i(x, y, 0.002) - c^i_{h,\Delta t}(x, y, 0.002)\|_{L^2(\Omega)},$$

for $i = 0, 1$, where the error norm is computed at the final time as $\|f\|^2_{L^2(\Omega)} = \int_\Omega f^2 \mathrm{d}\Omega$. As expected, the results exhibit optimal convergence rates of order $\mathcal{O}(h^{p+1})$, confirming the optimal performance of the FE-DIRK-Newton scheme with respect to the spatial discretization.

To study the convergence with respect to the time discretization, we consider a fixed fine mesh with mesh resolution of $n = 8$, element size $h = 2^{-7}$ mm, and elements of degree $p = 2$, a fixed time interval $I = [0, 2]$ hours, and decreasing time steps $\Delta t = 1, 2^{-1}, 2^{-2}, 2^{-3}$ hours. We analize the convergence with respect to four DIRK methods: the (first-order) backward Euler, the (second-order) midpoint rule, a three stages DIRK method of order three, and a DIRK method of order four. The corresponding Butcher table for these methods are given in Appendix B.

Fig. 6 shows the L_2-norm error evolution and, as can be seen, the expected convergence rate is again recovered.

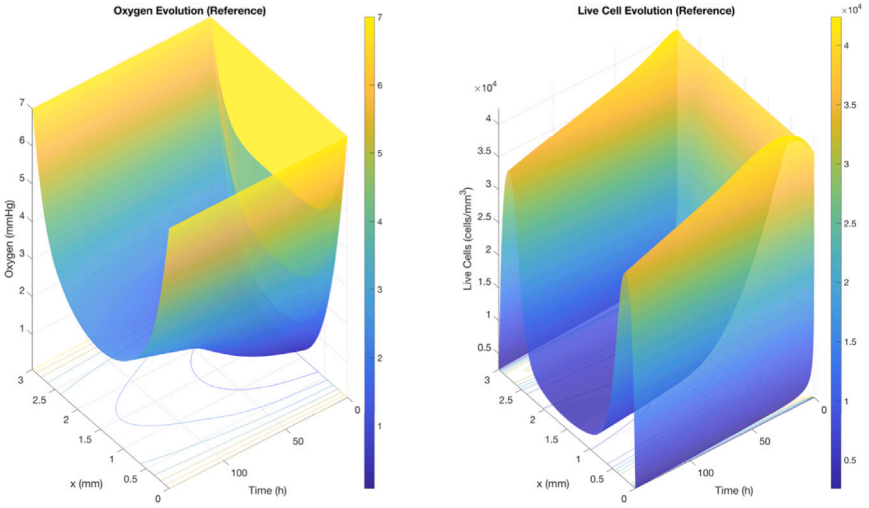

Fig. 7. Oxygen (left) and living cells (right) concentration evolution up to $t = 518\,000$ s, computed using a fine discretization to solve a one-dimensional problem.

4.2. Example 2: Reproduction of one-dimensional solution characteristics

This example assesses the ability of the proposed method to capture one-dimensional solution characteristics, consistent with previous studies on GBM progression. We consider the full coupled nonlinear system involving two cellular phenotypes and one chemical species, as summarized in Table 1, with model parameters defined in Table 2.

Two simulations are performed: one in a one-dimensional domain and the other in a two-dimensional setting. The one-dimensional domain is defined as $\Omega_1 = [0, L_x]$ with $L_x = 3$ mm. The corresponding two-dimensional domain is $\Omega_2 = [0, L_x] \times [0, L_y]$ with $L_y = 3$ mm. The time interval of interest for both simulations is approximately 6 days $I = [0, 5.18 \times 10^5]$ seconds.

The initial conditions in both cases as introduced in Eq. (6), are specified as follows: oxygen concentration $c^{0,0} = 7$ mmHg, living cell concentration $c^{1,0} = 4 \times 10^4$ cells/mm^3, and dead cell concentration $c^{2,0} = 0$ cells/mm^3.

For the one-dimensional case, we impose Dirichlet boundary conditions on oxygen at both endpoints: $c^0(0,t) = c^0(L_x,t) = 7$ mmHg. Robin boundary conditions are applied to the living cells at both ends:

$$f^1(0,t) = -\gamma\, c^1(0,t) \quad \text{and} \quad f^1(L_x,t), = \gamma c^1(L_x,t),$$

where f^1 denotes the corresponding boundary flux and $\gamma = 10^{-5}$ mm/s. No boundary condition is required for the ODE governing the dead cell population.

For the two-dimensional model, the same boundary conditions are prescribed on the left and right boundaries ($x = 0$ and $x = L_x$). Specifically, the values of c^0 and c^1 on $x = 0$ and $x = L_x$, are taken to be identical to those defined in the one-dimensional model. And to ensure that the solution of the two-dimensional model remains consistent with the one-dimensional case, we impose homogeneous Neumann boundary conditions on the top and bottom boundaries of the domain Ω_2, that is, $\boldsymbol{f}^1 \cdot \mathbf{n} = 0$. This setup allows for a direct comparison between the one-dimensional and two-dimensional simulations.

For the one-dimensional simulation, we use MATLAB's built-in function `pdepe`, which is tailored for solving small systems of parabolic partial differential equations in one spatial dimension and time. The solver is based on the method of lines (MOL), where a discretization with respect to space is introduced while the time variable remains continuous. This semidiscretization process transforms the PDE system into a system of ordinary differential equations (ODEs). In particular, the spatial discretization follows the method proposed by Skeel and Berzins [44], which is second-order accurate. Once discretized in space, the resulting system is integrated in time using `ode15s`, MATLAB's variable-order, variable-step stiff ODE solver based on backward differentiation formulas (BDFs). It is worth noting that the numerical method used for the one-dimensional simulation differs from the FE–DIRK–Newton formulation described throughout this article. Therefore, this example also enables a comparison between the proposed methodology and the results obtained with `pdepe`, thereby providing an independent numerical validation of the FE–DIRK–Newton formulation in a setting where the solution is expected to exhibit a purely one-dimensional character.

The one-dimensional case is solved using a very fine discretization, consisting of 3000 linear elements of length $\Delta x = 10^{-3}$ mm and 5180 time steps of $\Delta t = 100$ s. Fig. 7 shows the evolution obtained using `pdepe` built-in function for the concentration of oxygen and living cells, which are taken as reference solutions. It can be seen that the oxygen concentration remains constant at both ends of the spatial domain, while it decreases at the interior because of cell consumption. This descent in oxygen availability causes a decrease in the concentration of living cells, either because they die (due to the lack of oxygen) or migrate towards the domain limits, where oxygen levels are higher.

In the two-dimensional model, we use the midpoint rule with $\Delta t = 1000$ s and three different space discretizations of 30×30, 100×100 and 300×300 linear quadrilaterals, corresponding to element sizes $h = 0.1$ mm, $h = 0.03$ mm and $h = 0.01$ mm. Solving this two-dimensional formulation is computationally more demanding than the one-dimensional case. At each stage, a large nonlinear system must be solved. The system dimension depends on the spatial discretization: it is 1860 for $h = 0.1$ mm, 20 200 for $h = 0.03$ mm and 180 600 for $h = 0.01$ mm. Because the considered time step Δt is small, the Newton method converges within three or four iterations, although a larger number of iterations may be required during the initial time steps. In all considered cases, linear systems can be efficiently solved using a sparse direct solver. Despite the higher computational cost, it is important to note that the aim of this example is to validate the two-dimensional implementation rather than focus on numerical complexity.

Fig. 8 shows the oxygen and living cell concentrations at three different time instants ($t = 12$ h, $t = 24$ h and $t = 48$ h) for the reference solution along the straight line $y = 1.5$ mm for each of the three discretizations. The four solutions are nearly indistinguishable, except for small deviations in living cell concentration observed for the coarser mesh. To better visualize these differences, the right axes in each plot shows the absolute error of the concentrations with respect to the reference solution. Using the coarsest mesh, the error for the oxygen concentration is very small, less than 0.5%. The living cell concentration shows higher errors, reaching up to 15%, but only for the first and last elements of the mesh. Refining the mesh significantly reduces all errors across the entire domain.

Finally, Fig. 9 shows the error evolution for the three spatial discretizations. For all meshes, the first time steps show oxygen concentration errors up to 8%, which rapidly decrease and become negligible. In the case of living cell concentrations, the errors are localized near the spatial domain boundaries, where the solution shows a boundary layer behavior. These errors remain almost constant over time but they are reduced with mesh refinement.

4.3. Example 3: Three-dimensional simulation

In this example, we use our numerical model to simulate the behavior of two 3D microfluidic devices under two different experimental conditions, namely necrotic core formation and single palisade formation. To highlight the flexibility of the proposed formulation, in this example we use a spatial and temporal discretization that represents a compromise between accuracy and computational cost for the three-dimensional simulations. On the one hand, third-order hexahedral elements provide sufficient spatial resolution while using a coarse mesh with a small number of elements. On the other hand, the midpoint DIRK scheme ensures stability and second-order accuracy in time while using the same number of stages than first order backward Euler method.

Both devices have the same central chamber dimensions: $5.1 \times 0.3 \times 2$ mm. Fig. 10 shows the corresponding CAD models (Figs. 10(a) and 10(b)) and the two computational meshes (Figs. 10(c) and 10(d)). Their walls are shown in sky blue and are assumed to be impermeable. Each chamber is bounded by two inlet valves (shown in brown), used to infuse a mixture of collagen hydrogel, GBM living cells, and oxygen. Once the infusion process concludes, the valves are closed and treated as impermeable boundaries. Both devices also include multiple lateral exchange openings (shown in green) connecting the central chamber to two lateral channels that are used to supply oxygen at a constant rate. These openings may be opened or closed, depending on the specific experiment. The only difference between the two devices is the configuration of the lateral openings: the first device has five small openings per side, while the second has two larger openings per side. Despite this, the total lateral opening area per side is the same in both devices.

We discretize the CAD models using curved high-order hexahedral meshes generated using the methods proposed in [45,46]. The mesh for the first device consists of 2838 third-order elements and 87 100 nodes, while the mesh for the second one is composed of 2574 third-order elements and 79 060 nodes. The small differences in the meshes arise from the distinct geometrical configurations of the lateral openings. Note that, although the nature of the problem and the geometrical characteristics of the CAD model do not require the use of curved meshes, the mesh generator tends to deliver curved meshes in order to increase the quality of the final mesh.

The material parameters are the same in all cases and are listed in Table 2. They are consistent with those reported in [11,12]. The boundary conditions types are the same for both devices, and their values are summarized in Table 4. Specifically, for oxygen, we apply a Dirichlet boundary condition (prescribed oxygen concentration) at the active lateral openings and a homogeneous Neumann boundary condition (no-flux condition) on the solid walls, inlet valves and the inactive lateral openings. For living cells, we impose a Robin boundary condition on the active lateral openings and a homogeneous Neumann condition elsewhere. However, the specific values of the initial and boundary conditions differ between the two experiments.

In all simulations in this section, time integration is performed using the midpoint DIRK scheme with a time step $\Delta t = 0.2$ hours over the time interval of six days, namely $I = [0, 144]$ hours. Since midpoint DIRK scheme only involves one stage, only one non-linear system is posed per time step that is solved using Newton method. For all the 3D simulations we use the GMRES method with a diagonal preconditioner to solve the linear systems that are generated at each iteration of the Newton method.

Finally, in the numerical examples, we extract 1D solution profiles along two straight lines in the z-direction that passes through points $(x, y, z) = (1.56, 0.15, z)$ mm and $(x, y, z) = (2.52, 0.15, z)$ mm, respectively, as shown in Fig. 11.

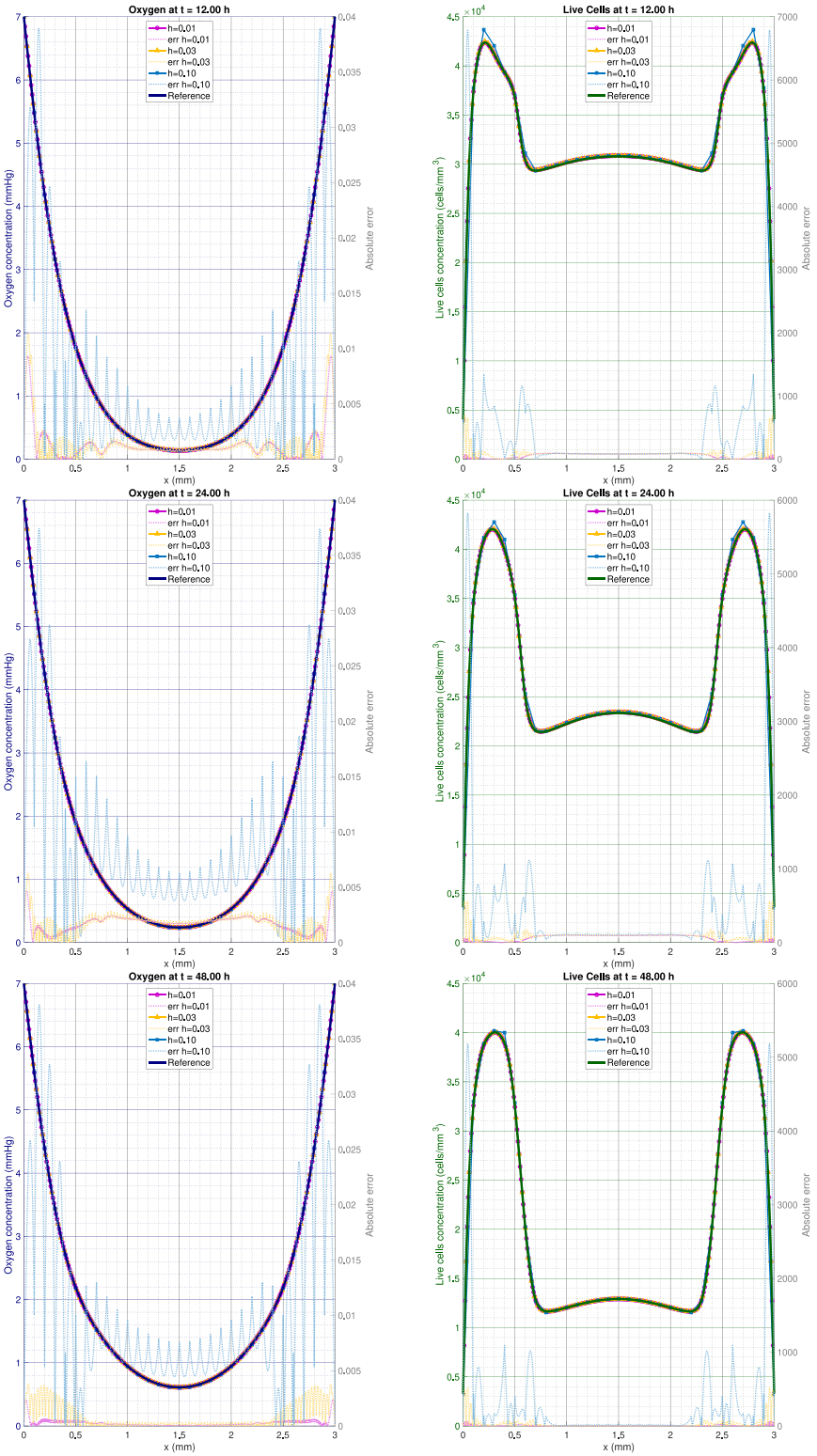

Fig. 8. Oxygen (left) and living cells (right) concentration at $t = 12$ h (top), $t = 24$ h (middle) and $t = 48$ h (bottom) for the one-dimensional solution and a cross at $y = 1.5$ mm for the two-dimensional solutions. The right axis shows the absolute error of all quantities (using the same units) with respect to the reference solution.

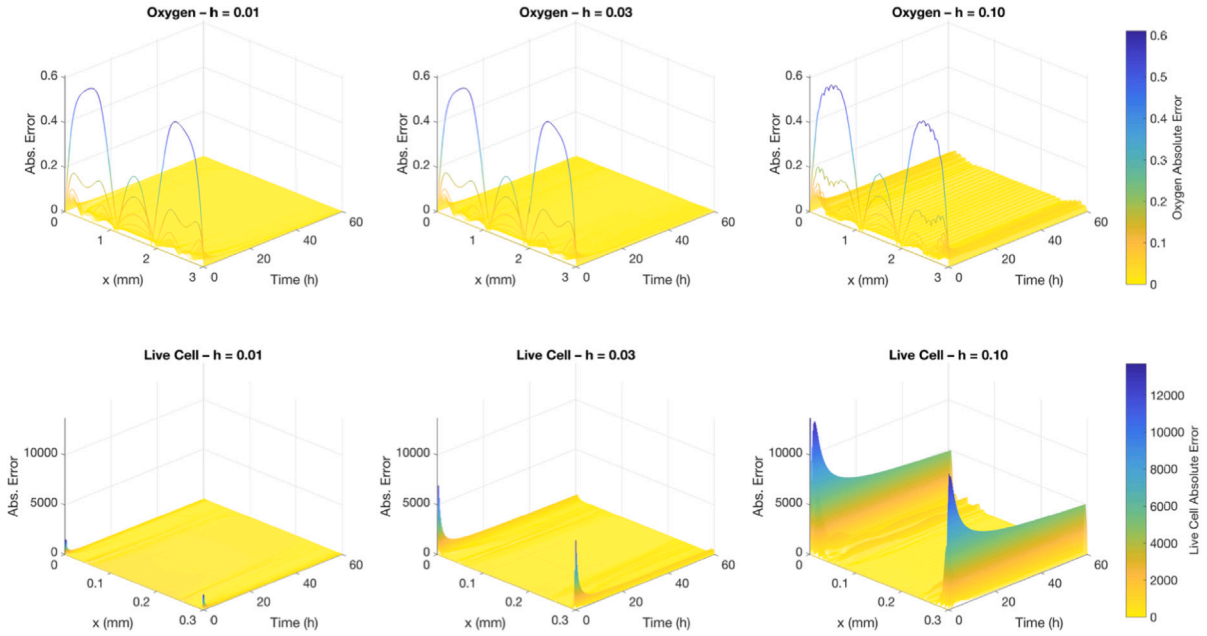

Fig. 9. Evolution of the absolute error (in absolute value) of the oxygen concentration [mmHg] and living cells concentration [cells/mm^3] up to $t = 216\,000$ s.

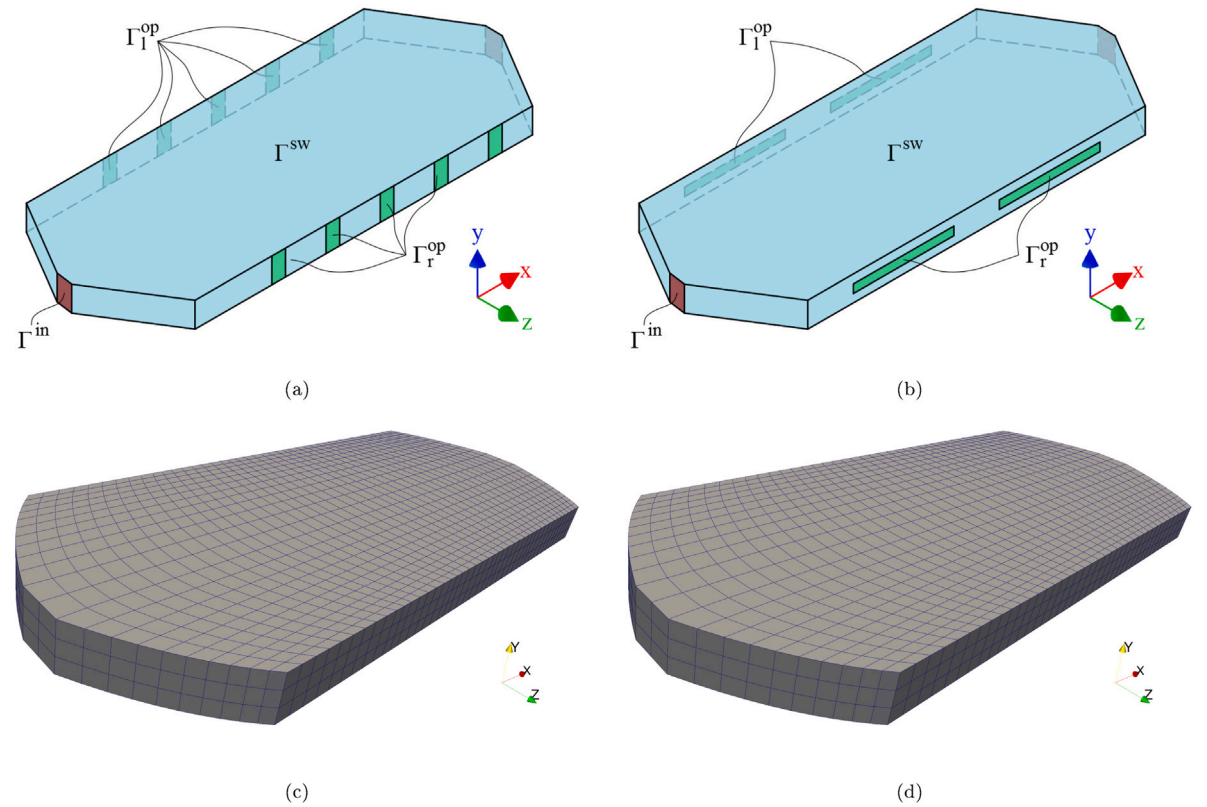

Fig. 10. 3D CAD models. Inlet valves Γ^{in} in brown, lateral openings $\Gamma^{op} = \Gamma_l^{op} \cup \Gamma_r^{op}$ in green and solid walls Γ^{sw} in blue. (a) microfluidic device with 5 holes per side; (b) microfluidic device with 2 holes per side; (c) curved third-order mesh for microfluidic device with 5 holes per side; and (d) curved third-order mesh for microfluidic device with 2 holes per side.

Table 4
Initial and boundary conditions for oxygen and living cells for the two working conditions. There are two major differences: the type of boundary conditions imposed on the left lateral openings Γ_l^{op}, which are only active in the necrotic core formation experiment, and the particular values of the boundary and initial conditions.

	Necrotic core formation		Single palisade	
Dirichlet BC	$\Gamma_D^0 = \Gamma_l^{op} \cup \Gamma_r^{op}$ $\Gamma_D^1 = \emptyset$	$g_D^0 = 7$ mmHg	$\Gamma_D^0 = \Gamma_r^{op}$ $\Gamma_D^1 = \emptyset$	$g_D^0 = 2$ mmHg
Neumann BC	$\Gamma_N^0 = \Gamma^{in} \cup \Gamma^{sw}$ $\Gamma_N^1 = \Gamma^{in} \cup \Gamma^{sw}$	$g_N^0 = 0$ mmHg/(mm^{2}s) $g_N^1 = 0$ cells/(mm^{2}s)	$\Gamma_N^0 = \Gamma^{in} \cup \Gamma^{sw} \cup \Gamma_l^{op}$ $\Gamma_N^1 = \Gamma^{in} \cup \Gamma^{sw} \cup \Gamma_l^{op}$	$g_N^0 = 0$ mmHg/(mm^{2}s) $g_N^1 = 0$ cells/(mm^{2}s)
Robin BC	$\Gamma_R^0 = \emptyset$ $\Gamma_R^1 = \Gamma_l^{op} \cup \Gamma_r^{op}$	$\gamma^1 = 10^{-5}$ mm/s $g_R^1 = 0$ cells/mm^3	$\Gamma_R^0 = \emptyset$ $\Gamma_R^1 = \Gamma_r^{op}$	$\gamma^1 = 10^{-8}$ mm/s $g_R^1 = 0$ cells/mm^3
Initial Conditions	$c^0(\boldsymbol{x}, 0) = 7$ mmHg $c^1(\boldsymbol{x}, 0) = 4 \times 10^4$ cells/mm^3		$c^0(\boldsymbol{x}, 0) = 2$ mmHg $c^1(\boldsymbol{x}, 0) = 4 \times 10^3$ cells/mm^3	

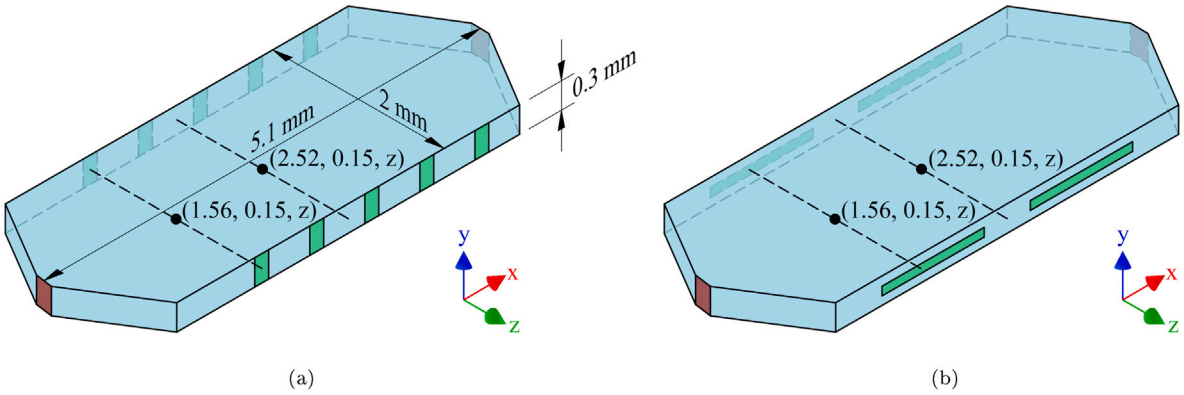

Fig. 11. The solution of the simulations will be plotted along the two straight lines that are displayed for (a) microfluidic device with 5 holes per side; (b) microfluidic device with 2 holes per side.

4.3.1. Necrotic core formation in 3D devices

In this experiment, the infused mixture contains a high concentration of oxygen and living cells, and no dead cells. The initial and boundary conditions are summarized in Table 4. Specifically, following [11,12] the initial conditions are defined as:

$$c^0(\boldsymbol{x}, 0) = 7 \text{ mmHg}, \qquad c^1(\boldsymbol{x}, 0) = 4 \times 10^4 \text{ cells/mm}^3, \qquad c^2(\boldsymbol{x}, 0) = 0 \text{ cells/mm}^3.$$

During the experiment, oxygen is supplied via the lateral openings located on both sides of the chamber. The applied boundary conditions are:

$$\begin{aligned}
c^0(\boldsymbol{x}, t) &= 7 \text{ mmHg} && \text{for } \boldsymbol{x} \in \Gamma_D^0 = \Gamma_l^{op} \cup \Gamma_r^{op}, \\
\boldsymbol{f}^0 \cdot \boldsymbol{n} &= 0 \text{ mmHg/(mm}^2 \text{ s)} && \text{for } \boldsymbol{x} \in \Gamma_N^0 = \Gamma^{in} \cup \Gamma^{sw}, \\
\boldsymbol{f}^1 \cdot \boldsymbol{n} &= \gamma^1 c^1(\boldsymbol{x}, t) && \text{for } \boldsymbol{x} \in \Gamma_R^1 = \Gamma_l^{op} \cup \Gamma_r^{op}, \\
\boldsymbol{f}^1 \cdot \boldsymbol{n} &= 0 \text{ cells/(mm}^2 \text{ s)} && \text{for } \boldsymbol{x} \in \Gamma_N^1 = \Gamma^{in} \cup \Gamma^{sw},
\end{aligned}$$

where $\gamma^1 = 10^{-5}$ mm/s is a hydrogel material property, see [11,12] for details.

Living cells consume the oxygen available in the infused mixture and proliferate. As oxygen is consumed, cells migrate towards regions of higher oxygen concentration, forming palisades of living cells near the lateral openings. These structures further hinder oxygen diffusion into the inner part of the central chamber, ultimately resulting in a necrotic core far from the lateral openings.

Fig. 12 presents the concentration of oxygen, living cells, and dead cells at time $t = 6$ days for both devices. As expected, oxygen concentration is higher at the lateral openings ($c^0 = 7$ mmHg) and decreases as we move towards the inner part of the central chamber due to its consumption by living cells (see Figs. 12(a) and 12(b)). Due to the cell migration towards more oxygenated regions, palisades of living cells form close to the lateral openings (see Figs. 12(c) and 12(d)). Since oxygen cannot reach the inner part of the central chamber, due to oxygen deprivation, dead cell concentration increases in this part of the chamber inducing the formation of a necrotic core (see Figs. 12(e) and 12(f)).

Fig. 13 shows the concentration of living cells for both devices in a $y - z$ cross-section located at $x = 1.56$ mm. While the five-hole device produces a homogeneous distribution of living cells in the y-direction (see Fig. 13(a)), the two-hole device produces inhomogeneous distributions of living cells in all three dimensions (see Fig. 13(b)). This highlights the need for a multidimensional

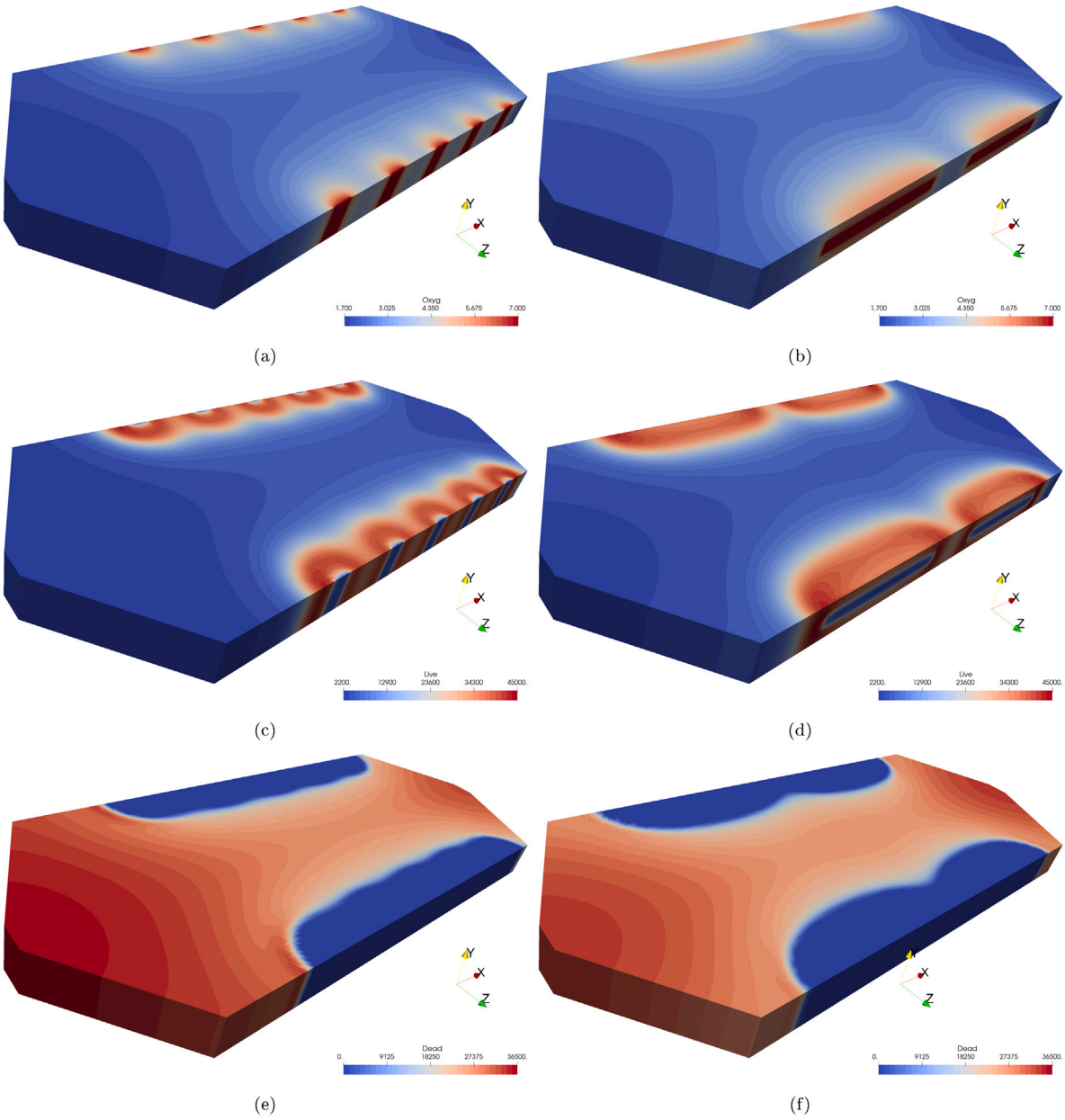

Fig. 12. Spatial distribution of the necrotic core formation after six days. Results for the microfluidic device with five small holes per side: (a) oxygen [mmHg]; (c) living cells [cells/mm^3]; (e) dead cells [cells/mm^3]. Results for the microfluidic device with two large holes per side: (b) oxygen [mmHg]; (d) living cells [cells/mm^3]; (f) dead cells [cells/mm^3].

numerical simulator. It is worth noting, that the device with five small openings generates palisades with a higher concentration of living cells and a more uniform necrotic core. These results are consistent with those reported in [11,12].

Fig. 14 compares 1D profiles of the concentrations of oxygen, living cells, and dead cells along the two lines in the z-direction shown in Fig. 11. Specifically, Fig. 14(a) presents the concentration profiles along the line $(x, y, z) = (1.56, 0.15, z)$ mm that corresponds to a line that passes through the center of the first lateral opening in the five-hole device. Fig. 14(b), in contrast, presents the concentration profiles along the line $(x, y, z) = (2.52, 0.15, z)$ mm that corresponds to a line located midway between the two lateral openings of the two-hole device. These plots reveal that the first device produces palisades and necrotic cores with higher concentrations of living and dead cells, respectively.

The total number of unknowns of the non-linear system (and the corresponding linear systems involved in the Newton method) is 173 500 for the CAD model with five lateral holes and 157 528 for the CAD with two lateral holes. For both CADs, three iterations of

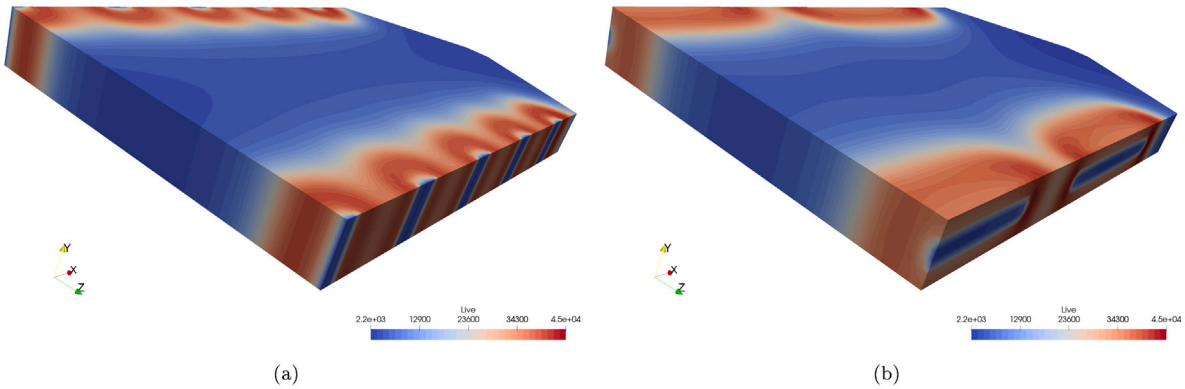

Fig. 13. Living cell concentration [cells/mm^3] on a plane located at $x = 1.56$ mm. (a) microfluidic device with five small holes; and (b) microfluidic device with two large holes.

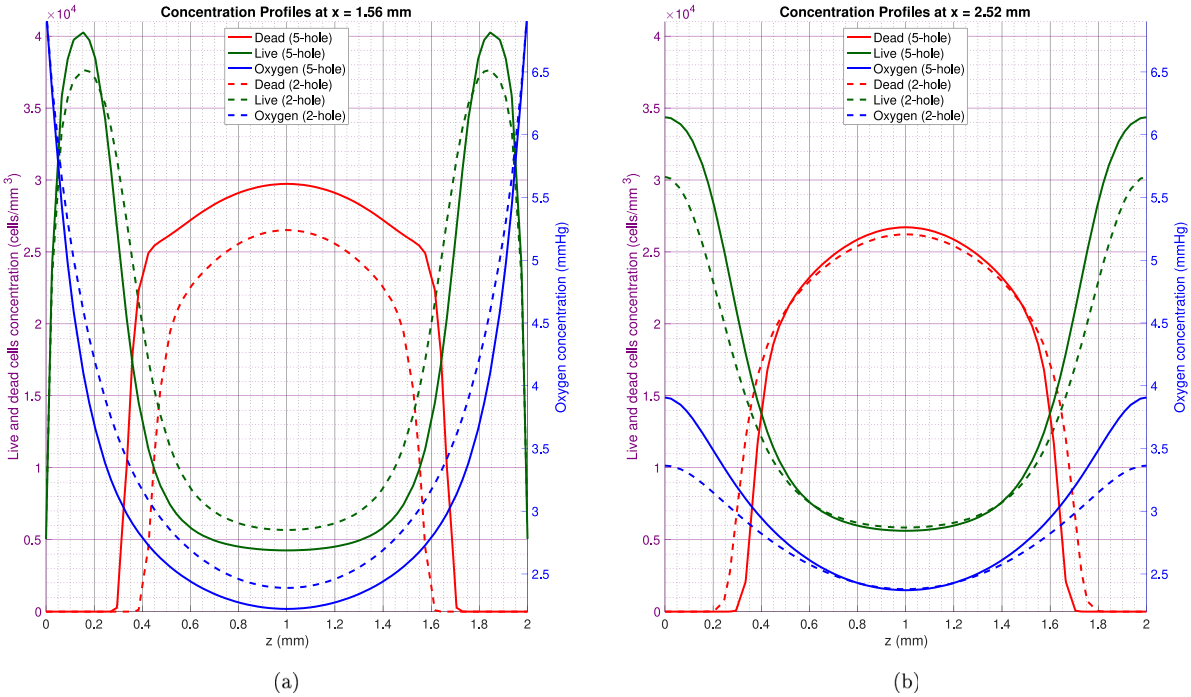

Fig. 14. Spatial distribution for the necrotic core experiment along a straight line in the z direction that passes through points: (a) $(x, y, z) = (1.56, 0.15, z)$ mm, and (b) $(x, y, z) = (2.52, 0.15, z)$ mm.

the Newton method were needed to achieve convergence. Only in the firsts time steps of the simulation four iteration were needed since we start from a constant initial condition. For the first model, the number of iterations of the diagonally preconditioned GMRES method ranges from 329 in the first iteration of the Newton method to 1 in the last one. Similarly, for the second model the number of iterations ranges from 323 in the first iteration of the Newton method to 1 in the last one. Note that for both models, in the first iteration of the Newton method a higher number of iterations of the GMRES is needed. This behavior clearly reflects the non-linear nature of the problem.

4.3.2. Single palisade formation in 3D devices

In this experiment, the infused mixture consists of a low concentration of oxygen and living cells, and no dead cells. The initial and boundary conditions are summarized in Table 4. Following the setup in [11,12], the initial conditions are defined as:

$$c^0(\boldsymbol{x}, 0) = 2 \text{ mmHg}, \qquad c^1(\boldsymbol{x}, 0) = 4 \times 10^3 \text{ cells/mm}^3, \qquad c^2(\boldsymbol{x}, 0) = 0 \text{ cells/mm}^3.$$

During the experiment, oxygen is supplied exclusively through the lateral openings located on the right side of the chamber. As in the previous experiment, Dirichlet boundary conditions are imposed for the oxygen and Robin boundary conditions for the living cells at these openings. In addition, the no-flux condition is enforced on all other parts of the boundary. The boundary conditions are:

$$\begin{aligned} c^0(\boldsymbol{x},t) &= \quad 2 \text{ mmHg} && \text{for } \boldsymbol{x} \in \Gamma_D^0 = \Gamma_{\mathrm{r}}^{\mathrm{op}}, \\ \boldsymbol{f}^0 \cdot \boldsymbol{n} &= \quad 0 \text{ mmHg/(mm}^2 \text{ s)} && \text{for } \boldsymbol{x} \in \Gamma_N^0 = \Gamma^{\mathrm{in}} \cup \Gamma^{\mathrm{sw}} \cup \Gamma_1^{\mathrm{op}}, \\ \boldsymbol{f}^1 \cdot \boldsymbol{n} &= \quad \gamma^1 c^1(\boldsymbol{x},t) && \text{for } \boldsymbol{x} \in \Gamma_R^1 = \Gamma_{\mathrm{r}}^{\mathrm{op}}, \\ \boldsymbol{f}^1 \cdot \boldsymbol{n} &= \quad 0 \text{ cells/(mm}^2 \text{ s)} && \text{for } \boldsymbol{x} \in \Gamma_N^1 = \Gamma^{\mathrm{in}} \cup \Gamma^{\mathrm{sw}} \cup \Gamma_1^{\mathrm{op}}, \end{aligned}$$

where $\gamma^1 = 10^{-8}$ mm/s is smaller compared to the previous experiment to reflect the different composition of the infused mixture (see [11,12] for details).

Fig. 15 shows the concentration of oxygen, living cells, and dead cells at time $t = 9$ days for both microfluidic device configurations. As in the previous experiment, the oxygen concentration reaches its maximum at the lateral openings (now located only on the right side of the central chamber) and decreases with increasing distance from these openings, see Figs. 15(a) and 15(b).

In this case, the initial concentrations of oxygen and living cells are much lower than in the necrotic core experiment. As a result, the living cell concentration remains significantly below the saturation threshold, $c_s^1 = 5 \times 10^4$ cells/mm^3, and the oxygen concentration is also below the hypoxia migration threshold, $c_h^0 = 7$ mmHg. Consequently, the combined effect of chemotaxis, saturation and proliferation is less important in this experiment, and living cells do not strongly migrate in the direction of the oxygen gradient. This leads to the formation of a palisade with considerably lower maximum concentration ($c^1 = 1.3{\times}10^4$ cells/mm^3) compared to the previous experiment ($c^1 = 4.5 \times 10^4$ cells/mm^3), as seen in Figs. 15(c) and 15(d).

Due to the reduced oxygen demand of living cells, oxygen supplied through the openings can reach the inner regions of the chamber. As a result, the medium maintains oxygen levels that are sufficient for the survival of living cells, reducing chemotaxis flow and leading to a smaller and less severe necrotic core ($c^2 = 4.9 \times 10^3$ cells/mm^3) compared to the previous setup ($c^2 = 3.6 \times 10^4$ cells/mm^3), as shown in Figs. 15(e) and 15(f).

Fig. 16 presents 1D profiles of oxygen, living cells, and dead cells along the two lines in the z-direction shown in Fig. 11. It should be noted that the concentration of dead cells reaches a plateau far from the oxygen inlets (lateral openings). Moreover, when comparing the single palisade case (Fig. 16(a)) with the necrotic core experiment (Fig. 14(a)), the influence of the Robin boundary condition becomes evident. In this setup, due to the lower values of c^1 and γ^1, the effect of the boundary condition is significantly reduced.

Finally, it is worth highlighting that, unlike in the necrotic core formation experiment, in this case both devices exhibit similar behavior. This demonstrates the importance of the proposed numerical model and its ability to predict the response of GBM cell cultures in microfluidic devices under experimental setups to mimic different physiological conditions.

For this experiment, the total number of unknowns is 173 850 for the CAD model with five lateral holes and 157 824 for the CAD with two lateral holes. Note that the number of unknowns is slightly higher in this experiment than in the previous one because homogeneous Neumann conditions are also prescribed for oxygen on all of the lateral openings of one side of the microfluidic device. For both models, and similar to the previous experiment, three iterations of the Newton method were needed to achieve convergence and only four iterations were required in the firsts time steps of the simulation. For the first model, the number of iterations of the diagonally preconditioned GMRES method ranges from 332 in the first iteration of the Newton method to 1 in the last one. For the second model the number of iterations ranges from 328 to 1 iterations.

5. Conclusions and future work

In this work, we have presented a numerical framework for simulating the progression of glioblastoma (GBM) cells within microfluidic devices. The model accounts for two key cell phenotypes — living and dead cells — and a critical nutrient, oxygen, enabling the prediction of tumor behavior under a wide range of experimental configurations. The approach is designed to support the analysis of cell cultures in novel microfluidic device designs and to evaluate new working hypotheses related to GBM growth and oxygen availability and dosage.

The proposed mathematical model consists of a coupled nonlinear system: two transient partial differential equations for oxygen and living cells, and a partial differential equation for dead cells, which lacks spatial derivatives reducing to a family of ordinary differential equations, which is solved pointwise in space. A continuous Galerkin formulation is employed in space, combined with a Diagonally Implicit Runge–Kutta (DIRK) method for time integration. The coupled oxygen–living cell nonlinear system is solved using Newton's method. Once the oxygen–living cell concentrations are computed, the dead cell concentration is computed.

We have verified the implementation of the method and illustrated the applicability of the model through several examples. First, we confirmed spatial and temporal convergence using a manufactured solution, verifying that our method reproduces the expected convergence rates, both in space and time. Second, we validated the model by reproducing known results from a 1D model [11] using a 2D synthetic geometry, demonstrating the ability of the framework to quantitatively replicate established biological patterns such as necrotic core formation and living cell palisade, the main histopathological features of GBM. Finally, we have applied the method to simulate 3D geometries of real microfluidic devices and captured two experimentally observed behaviors: necrotic core formation when oxygen is supplied from both sides of the chamber and the emergence of a single palisade when oxygen is provided from only one side. Beyond reproducing the results of previous 1D models [11], extending the framework to 2D and 3D enables the

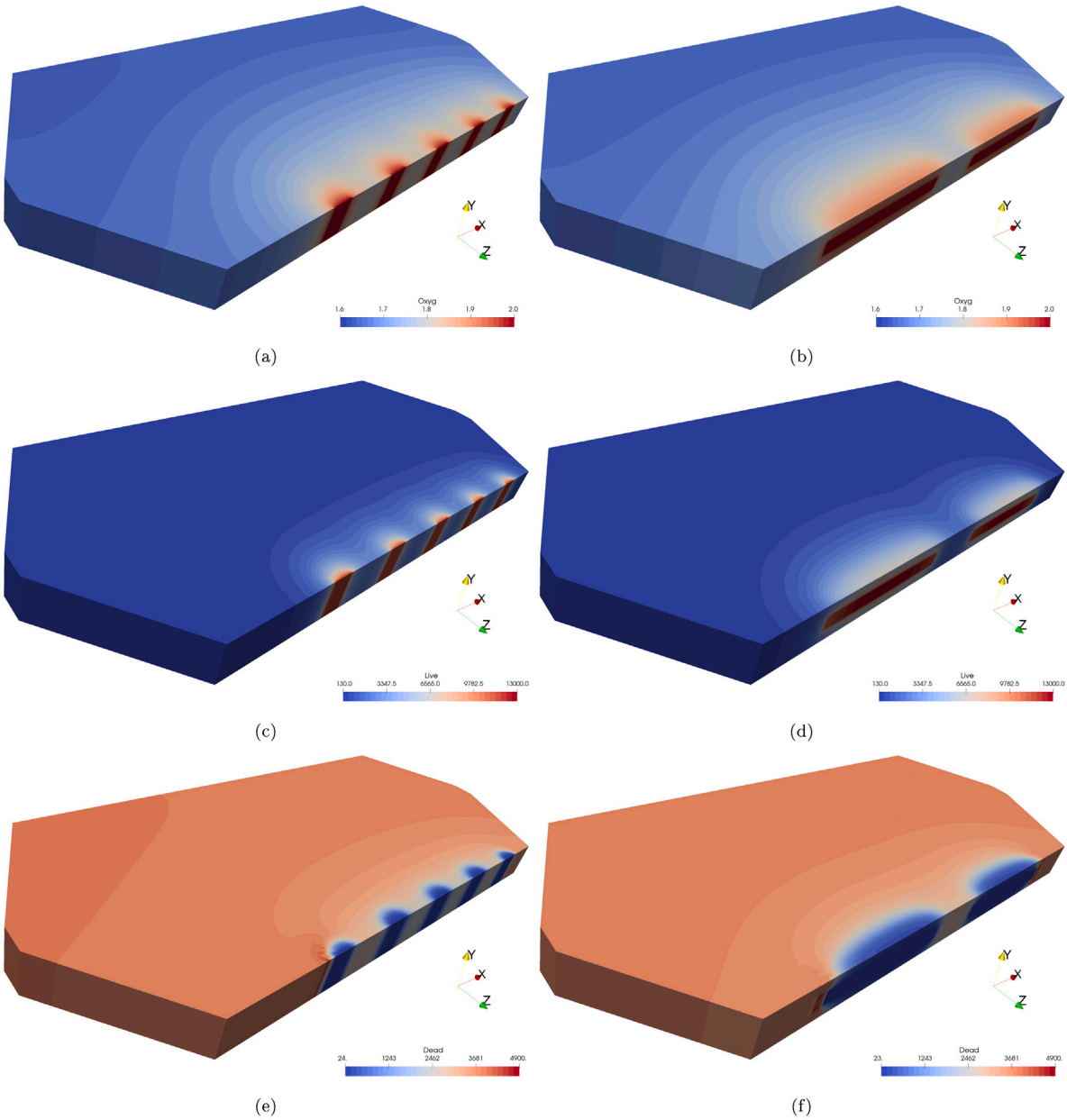

Fig. 15. Spatial distribution for the single palisade formation after nine days. Results for the microfluidic device with five small holes in one side: (a) oxygen; (c) living cells; (e) dead cells. Results for the microfluidic device with two large holes in one side: (b) oxygen; (d) living cells; (f) dead cells.

inclusion of realistic geometrical features of the experimental setup, such as the microfluidic chamber shape and the oxygen supply through the gaps between pillars, which cannot be captured in 1D models, thus allowing the exploration of phenomena driven by spatial anisotropy.

The methodology introduced in this work is both flexible and extensible. On the modeling side, the inclusion of drug dosage is a natural extension that will allow simulating other therapy scenarios. This will introduce a new equation into the system (similar to the oxygen equation) and increase the size of the nonlinear problem to be solved at each DIRK stage. On the numerical side, future work will focus on improving computational efficiency by developing a Hybridizable Discontinuous Galerkin (HDG) formulation. This will require special treatment of the nonlinear chemotaxis terms for the living cell equation, but will significantly reduce the number of global degrees of freedom.

Additionally, we aim to explore staggered time integration strategies in which oxygen and living cell concentrations are updated in sequence rather than simultaneously. Such approaches can reduce the size of linear systems at each stage and enable the use of

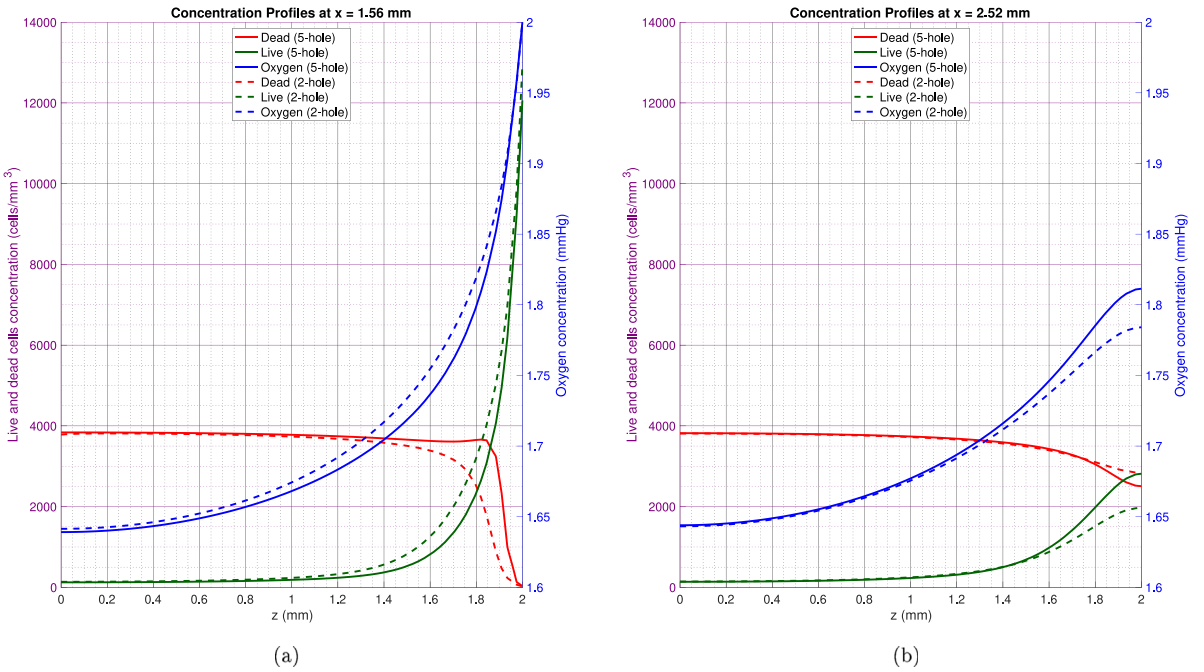

Fig. 16. Spatial distribution for the single palisade experiment along a straight line in the z direction that passes through points: (a) $(x, y, z) = (1.56, 0.15, z)$ mm, and (b) $(x, y, z) = (2.52, 0.15, z)$ mm.

tailored iterative solvers. This is especially relevant given the significant difference in scale between oxygen and tumor cell transport properties, with several orders of magnitude separating the oxygen diffusivity from the diffusivity and chemotaxis coefficient of living cells. Finally, we will assess the use of fixed-point iteration as a lower-cost alternative to 's method in regimes where nonlinearities are moderate. Altogether, this work lays the foundation for robust and predictive simulation of tumor growth in high-dimensional settings, extending the capabilities of earlier 1D models to 2D and 3D geometries. This advancement supports more realistic *in vitro* replication and enhances the potential for *in silico* experimentation in glioblastoma research.

CRediT authorship contribution statement

E. Sala-Lardies: Writing – review & editing, Writing – original draft, Software, Formal analysis. **J. Sarrate:** Writing – review & editing, Writing – original draft, Software, Funding acquisition, Formal analysis. **M. Pérez-Aliacar:** Writing – review & editing, Writing – original draft, Formal analysis, Conceptualization. **J. Ayensa-Jiménez:** Writing – review & editing, Writing – original draft, Formal analysis, Conceptualization. **M. Doblaré:** Writing – review & editing, Writing – original draft, Funding acquisition, Formal analysis, Conceptualization. **N. Parés:** Writing – review & editing, Writing – original draft, Software, Formal analysis.

Declaration of competing interest

The authors declare that they have no known competing financial interests or personal relationships that could have appeared to influence the work reported in this paper.

Acknowledgments

This work has been supported by FEDER, Spain and the Spanish Government, Ministerio de Ciencia e Innovación under grant project contracts PID2021-126051OB-C41, PID2021-126051OB-C44 and TED2021-129512B-I00. Manuel Doblaré acknowledges the financial support from Beonchip S.L through the project DIAMOOC IDI-20220819.

Appendix A. The FE-DIRK-Newton method: detailed residuals and Jacobian matrices

At each stage of the DIRK method described in Section 3.3, the nonlinear coupled system of equations given in (30) is first solved to determine the oxygen and living cells concentrations, $c_h^{0,n,l}$ and $c_h^{1,n,l}$ respectively. Once these concentrations are available, the uncoupled linear system of equations given in (31) is solved to find the concentration of dead cells, $c_h^{2,n,l}$. Recall that $c_h^{0,n,l}$, $c_h^{1,n,l}$ and

$\boldsymbol{c}_h^{2,n,l}$ are the vectors containing the nodal unknowns of the concentrations at time $t^{n,l}$, evaluated at the mesh nodes $\boldsymbol{x}_j$, for $j \in \mathcal{N}^i$. That is, as shown in Eq. (22),

$$\boldsymbol{c}_h^{i,n,l} = [c_{hj}^{i,n,l}]_{j\in\mathcal{N}^i} \quad \text{where} \quad c_{hj}^{i,n,l} \approx c_{hj}^i(t^{n,l}) = c_h^i(\boldsymbol{x}_j, t^{n,l}).$$

Using these notations and Eq. (24), the explicit form of the residual equation for dead cells given in Eq. (31) at time stage $t^{n,l}$ becomes:

$$\frac{c_{hj}^{2,n,l} - \hat{c}_{hj}^{2,n,l}}{\Delta t\, a_{ll}} - s^2(c_{hj}^{0,n,l}, c_{hj}^{1,n,l}) = 0,$$

which leads to the expression:

$$c_{hj}^{2,n,l} = \hat{c}_{hj}^{2,n,l} + \Delta t\, a_{ll} s^2(c_{hj}^{0,n,l}, c_{hj}^{1,n,l}).$$

However, to compute the concentrations at the next time step t^{n+1} using Eq. (27), only the time derivatives of the concentrations are required. Therefore, it is sufficient to directly evaluate the derivatives using Eq. (24) as:

$$\dot{c}_{hj}^{2,n,l} = s^2(c_{hj}^{0,n,l}, c_{hj}^{1,n,l}).$$

Regarding the coupled residual for oxygen and living cells defined in Eq. (30), recall that it may be rewritten by introducing the stage residual vectors $\boldsymbol{R}^{0,n,l}$ and $\boldsymbol{R}^{1,n,l}$, as shown in Eq. (34). Then, recalling the notation for the discrete nodal residuals $\boldsymbol{R}^{0,n,l} = [R_\alpha^{0,n,l}]_{\alpha\in\mathcal{N}^0}$ and $\boldsymbol{R}^{1,n,l} = [R_\alpha^{1,n,l}]_{\alpha\in\mathcal{N}^1}$, it follows that

$$\begin{aligned}
R_\alpha^{0,n,l} &= \sum_{j=1}^{n_{\text{np}}} \frac{c_{hj}^{0,n,l} - \hat{c}_{hj}^{0,n,l}}{\Delta t\, a_{ll}} \int_\Omega N_j N_\alpha \,\mathrm{d}\Omega + \sum_{j=1}^{n_{\text{np}}} c_{hj}^{0,n,l} \int_\Omega \boldsymbol{A}^0 \boldsymbol{\nabla} N_j \cdot \boldsymbol{\nabla} N_\alpha \,\mathrm{d}\Omega + \sum_{j=1}^{n_{\text{np}}} c_{hj}^{0,n,l} \int_{\Gamma_R^0} \gamma^0 N_j N_\alpha \,\mathrm{d}\Gamma \\
&\quad - \int_\Omega s^0(c_h^{0,n,l}, c_h^{1,n,l}) N_\alpha \,\mathrm{d}\Omega + \int_{\Gamma_N^0} g_N^0 N_\alpha \,\mathrm{d}\Gamma - \int_{\Gamma_R^0} \gamma^0 g_R^0 N_\alpha \,\mathrm{d}\Gamma \qquad \text{for } \alpha \in \mathcal{N}^0, \\
R_\alpha^{1,n,l} &= \sum_{j=1}^{n_{\text{np}}} \frac{c_{hj}^{1,n,l} - \hat{c}_{hj}^{1,n,l}}{\Delta t\, a_{ll}} \int_\Omega N_j N_\alpha \,\mathrm{d}\Omega + \sum_{j=1}^{n_{\text{np}}} c_{hj}^{1,n,l} \int_\Omega \boldsymbol{A}^1 \boldsymbol{\nabla} N_j \cdot \boldsymbol{\nabla} N_\alpha \,\mathrm{d}\Omega \\
&\quad - \sum_{r=1}^{n_{\text{np}}} \sum_{j=1}^{n_{\text{np}}} c_{hj}^{1,n,l} c_{hr}^{0,n,l} \int_\Omega N_j \boldsymbol{B}^{10}(c_h^{0,n,l}, c_h^{1,n,l}) \boldsymbol{\nabla} N_r \cdot \boldsymbol{\nabla} N_\alpha \,\mathrm{d}\Omega + \sum_{j=1}^{n_{\text{np}}} c_{hj}^{1,n,l} \int_{\Gamma_R^1} \gamma^1 N_j N_\alpha \,\mathrm{d}\Gamma \\
&\quad - \int_\Omega s^1(c_h^{0,n,l}, c_h^{1,n,l}) N_\alpha \,\mathrm{d}\Omega + \int_{\Gamma_N^1} g_N^1 N_\alpha \,\mathrm{d}\Gamma - \int_{\Gamma_R^1} \gamma^1 g_R^1 N_\alpha \,\mathrm{d}\Gamma \qquad \text{for } \alpha \in \mathcal{N}^1,
\end{aligned}$$

where analogously to Eq. (20) the concentrations at each stage are given by

$$c_h^{i,n,l}(\boldsymbol{x}) = \sum_{j=1}^{n_{\text{np}}} N_j(\boldsymbol{x}) c_{hj}^{i,n,l} = \sum_{j\in\mathcal{D}^i} N_j(\boldsymbol{x}) g_D^i(\boldsymbol{x}_j) + \sum_{j\in\mathcal{N}^i} N_j(\boldsymbol{x}) c_{hj}^{i,n,l}. \tag{A.1}$$

From these expressions, the specific formulas of the Jacobian blocks $\partial_j \boldsymbol{R}^{i,n,l}$ defined in Eq. (36) may be derived, recalling that

$$\left[\partial_j \boldsymbol{R}^{i,n,l}\right]_{\alpha\beta} = \left[\frac{\partial \boldsymbol{R}^{i,n,l}}{\partial \boldsymbol{c}_h^{j,n,l}}\right]_{\alpha\beta} = \frac{\partial R_\alpha^{i,n,l}}{\partial c_{h\beta}^{j,n,l}}, \qquad \text{for } i,j = 0,1 \text{ and } \alpha \in \mathcal{N}^i, \beta \in \mathcal{N}^j, \tag{A.2}$$

where $c_{h\beta}^{j,n,l}$ are the nodal values of $\boldsymbol{c}_h^{j,n,l}$ at the nodal points $\boldsymbol{x}_\beta$, $\boldsymbol{c}_h^{j,n,l} = [c_{h\beta}^{j,n,l}]_{\beta\in\mathcal{N}^j}$. Specifically:

$$\begin{aligned}
\left[\partial_0 \boldsymbol{R}^{0,n,l}\left(\boldsymbol{c}_h^{0,n,l}, \boldsymbol{c}_h^{1,n,l}\right)\right]_{\alpha\beta} &= \frac{\partial R_\alpha^{0,n,l}}{\partial c_{h\beta}^{0,n,l}} = \frac{1}{\Delta t\, a_{ll}} \int_\Omega N_\beta N_\alpha \,\mathrm{d}\Omega + \int_\Omega \boldsymbol{A}^0 \boldsymbol{\nabla} N_\beta \cdot \boldsymbol{\nabla} N_\alpha \,\mathrm{d}\Omega + \int_{\Gamma_R^0} \gamma^0 N_\beta N_\alpha \,\mathrm{d}\Gamma \\
&\quad + \int_\Omega \alpha_*^{01} \frac{c_m^0}{(c_h^{0,n,l} + c_m^0)^2} c_h^{1,n,l} N_\beta N_\alpha \,\mathrm{d}\Omega, \\
\left[\partial_1 \boldsymbol{R}^{0,n,l}\left(\boldsymbol{c}_h^{0,n,l}, \boldsymbol{c}_h^{1,n,l}\right)\right]_{\alpha\beta} &= \frac{\partial R_\alpha^{0,n,l}}{\partial c_{h\beta}^{1,n,l}} = \int_\Omega \alpha_*^{01} \frac{c_h^{0,n,l}}{c_h^{0,n,l} + c_m^0} N_\beta N_\alpha \,\mathrm{d}\Omega,
\end{aligned}$$

$$\left[\partial_0 \boldsymbol{R}^{1,n,l}\left(\boldsymbol{c}_h^{0,n,l},\boldsymbol{c}_h^{1,n,l}\right)\right]_{\alpha\beta} = \frac{\partial R_\alpha^{1,n,l}}{\partial c_{h\beta}^{0,n,l}}$$

$$= -\sum_{r=1}^{n_{\mathrm{np}}}\sum_{j=1}^{n_{\mathrm{np}}} c_{hj}^{1,n,l}\, c_{hr}^{0,n,l} \int_\Omega N_j B_*^{10}\, \dot{\psi}_-(c_h^{0,n,l};c_h^0)\, \psi_-(c_h^{1,n,l};c_s^1) N_\beta \boldsymbol{\nabla} N_r \cdot \boldsymbol{\nabla} N_\alpha \,\mathrm{d}\Omega$$

$$- \sum_{j=1}^{n_{\mathrm{np}}} c_{hj}^{1,n,l}\, c_{h\beta}^{0,n,l} \int_\Omega N_j B_*^{10}\, \psi_-(c_h^{0,n,l};c_h^0)\, \psi_-(c_h^{1,n,l};c_s^1) \boldsymbol{\nabla} N_\beta \cdot \boldsymbol{\nabla} N_\alpha \,\mathrm{d}\Omega$$

$$- \int_\Omega \left(\frac{1}{\tau_*^{11}} \dot{\psi}_+(c_h^{0,n,l};c_h^0)\, \psi_-(c_h^{1,n,l};c_s^1) c_h^{1,n,l} + \frac{1}{\tau_*^{12}} \dot{\chi}(c_h^{0,n,l};c_a^0,\Delta c_a^0) c_h^{1,n,l} \right) N_\beta N_\alpha \,\mathrm{d}\Omega,$$

$$\left[\partial_1 \boldsymbol{R}^{1,n,l}\left(\boldsymbol{c}_h^{0,n,l},\boldsymbol{c}_h^{1,n,l}\right)\right]_{\alpha\beta} = \frac{\partial R_\alpha^{1,n,l}}{\partial c_{h\beta}^{1,n,l}} = \frac{1}{\Delta t\, a_{ll}} \int_\Omega N_\beta N_\alpha \,\mathrm{d}\Omega + \int_\Omega \boldsymbol{A}^1 \boldsymbol{\nabla} N_\beta \cdot \boldsymbol{\nabla} N_\alpha \,\mathrm{d}\Omega + \int_{\Gamma_R^1} \gamma^1 N_\beta N_\alpha \,\mathrm{d}\Gamma$$

$$- \sum_{r=1}^{n_{\mathrm{np}}} c_{hr}^{0,n,l} \int_\Omega N_\beta B_*^{10}\, \psi_-(c_h^{0,n,l};c_h^0)\, \psi_-(c_h^{1,n,l};c_s^1) \boldsymbol{\nabla} N_r \cdot \boldsymbol{\nabla} N_\alpha \,\mathrm{d}\Omega$$

$$- \sum_{r=1}^{n_{\mathrm{np}}}\sum_{j=1}^{n_{\mathrm{np}}} c_{hj}^{1,n,l}\, c_{hr}^{0,n,l} \int_\Omega N_j B_*^{10}\, \psi_-(c_h^{0,n,l};c_h^0)\, \dot{\psi}_-(c_h^{1,n,l};c_s^1) N_\beta \boldsymbol{\nabla} N_r \cdot \boldsymbol{\nabla} N_\alpha \,\mathrm{d}\Omega$$

$$- \int_\Omega \frac{1}{\tau_*^{11}} \psi_+(c_h^{0,n,l};c_h^0) \left(\dot{\psi}_-(c_h^{1,n,l};c_s^1) c_h^{1,n,l} + \psi_-(c_h^{1,n,l};c_s^1) \right) N_\beta N_\alpha \,\mathrm{d}\Omega$$

$$- \int_\Omega \frac{1}{\tau_*^{12}} \chi(c_h^{0,n,l};c_a^0,\Delta c_a^0) N_\beta N_\alpha \,\mathrm{d}\Omega.$$

Appendix B. Butcher table for DIRK schemes used in this work

The time discretization of the PDE systems in this work is performed using Diagonally Implicit Runge–Kutta (DIRK) schemes. These methods are particularly suited for stiff problems due to their stability properties and the reduced cost associated with solving implicit stages compared to fully implicit Runge–Kutta methods.

For a detailed derivation and further theoretical background, we refer the reader to [16–19,47]. For completeness, next, we include the Butcher table of the DIRK schemes used in our numerical simulations.

- **Implicit Backward Euler (DIRK1-s1)**: A first-order single-stage method often used for its robustness and simplicity.

1	1
	1

- **Implicit Midpoint Rule (DIRK2-s1)**: A second-order, single-stage method with improved accuracy.

1/2	1/2
	1

- **DIRK3-s3**: A third-order, three-stage method based on a free parameter γ.

γ	γ	0	0
$\frac{1}{2}(1+\gamma)$	$\frac{1}{2}(1-\gamma)$	γ	0
1	$\frac{1}{4}(-6\gamma^2+16\gamma-1)$	$\frac{1}{4}(6\gamma^2-20\gamma+5)$	γ
	$\frac{1}{4}(-6\gamma^2+16\gamma-1)$	$\frac{1}{4}(6\gamma^2-20\gamma+5)$	γ

Here, as explained in [18], the optimal value is $\gamma = 0.4358665215$, which is the central solution of the equation:

$$\frac{1}{6} - \frac{3}{2}\gamma + 3\gamma^2 - \gamma^3 = 0.$$

- **DIRK4-s6**: A fourth-order, six-stage scheme proposed in [47].

0.079672377876931	0.079672377876931					
0.464364648310935	0.328355391763968	0.136009256546967				
1.348559241946724	-0.650772774016417	1.742859063495349	0.256472952467792			
1.312664210308764	-0.714580550967259	1.793745752775934	-0.078254785672497	0.311753794172585		
0.989469293495897	-1.120092779092918	1.983452339867353	3.117393885836001	-3.761930177913743	0.770646024799205	
1	0.214823667785537	0.536367363903245	0.154488125726409	-0.217748592703941	0.072226422925896	0.239843012362853
	0.214823667785537	0.536367363903245	0.154488125726409	-0.217748592703941	0.072226422925896	0.239843012362853

Data availability

Data will be made available on request.

References

[1] D.J. Brat, Glioblastoma: biology, genetics, and behavior, Am. Soc. Clin. Oncol. Educ. Book 32 (1) (2012) 102–107.
[2] T. Oike, Y. Suzuki, K. Sugawara, K. Shirai, S. Noda, T. Tamaki, M. Nagaishi, H. Yokoo, Y. Nakazato, T. Nakano, Radiotherapy plus concomitant adjuvant temozolomide for glioblastoma: Japanese mono-institutional results, PloS One 8 (11) (2013) e78943.
[3] L. Bonosi, S. Marrone, U.E. Benigno, F. Buscemi, S. Musso, M. Porzio, M.P. Silven, F. Torregrossa, G.M. Grasso, Maximal safe resection in glioblastoma surgery: A systematic review of advanced intraoperative image-guided techniques, Brain Sci. 13 (2) (2023) 216.
[4] W. Diao, X. Tong, C. Yang, F. Zhang, C. Bao, H. Chen, L. Liu, M. Li, F. Ye, Q. Fan, et al., Behaviors of glioblastoma cells in in vitro microenvironments, Sci. Rep. 9 (1) (2019) 85.
[5] E.K. Sackmann, A.L. Fulton, D.J. Beebe, The present and future role of microfluidics in biomedical research, Nature 507 (7491) (2014) 181–189.
[6] S.N. Bhatia, D.E. Ingber, Microfluidic organs-on-chips, Nature Biotechnol. 32 (8) (2014) 760–772.
[7] X. Cai, R.G. Briggs, H.B. Homburg, I.M. Young, E.J. Davis, Y.-H. Lin, J.D. Battiste, M.E. Sughrue, Application of microfluidic devices for glioblastoma study: Current status and future directions, Biomed. Microdevices 22 (3) (2020) 60.
[8] A. Martínez-González, G.F. Calvo, L.A. Pérez Romasanta, V.M. Pérez-García, Hypoxic cell waves around necrotic cores in glioblastoma: a biomathematical model and its therapeutic implications, Bull. Math. Biol. 74 (2012) 2875–2896.
[9] J.M. Ayuso, M. Virumbrales-Muñoz, A. Lacueva, P.M. Lanuza, E. Checa-Chavarria, P. Botella, E. Fernández, M. Doblare, S.J. Allison, R.M. Phillips, et al., Development and characterization of a microfluidic model of the tumour microenvironment, Sci. Rep. 6 (1) (2016) 36086.
[10] J.M. Ayuso, R. Monge, A. Martínez-González, M. Virumbrales-Muñoz, G.A. Llamazares, J. Berganzo, A. Hernández-Laín, J. Santolaria, M. Doblaré, C. Hubert, et al., Glioblastoma on a microfluidic chip: Generating pseudopalisades and enhancing aggressiveness through blood vessel obstruction events, Neuro-Oncol. 19 (4) (2017) 503–513.
[11] J. Ayensa-Jimeńez, M. Pérez-Aliacar, T. Randelovic, J.A. Sanz-Herrera, M.H. Doweidar, M. Doblare, Mathematical formulation and parametric analysis of in vitro cell models in microfluidic devices: application to different stages of glioblastoma evolution, Sci. Rep. 10 (1) (2020) 1–21.
[12] J. Ayensa-Jimeńez, M. Pérez-Aliacar, T. Randelovic, J.A. Sanz-Herrera, M.H. Doweidar, M. Doblare, Analysis of the parametric correlation in mathematical modeling of in vitro glioblastoma evolution using copulas, Mathematics 9 (1) (2020) 27.
[13] M.O. Deville, P.F. Fischer, E.H. Mund, High-Order Methods for Incompressible Fluid Flow, vol. 9, Cambridge University Press, 2002.
[14] G. Karniadakis, S. Sherwin, Spectral/hp Element Methods for Computational Fluid Dynamics, Numerical Mathematics and Scie, 2005.
[15] C. Schwab, p-and hp-Finite Element Methods: Theory and Applications in Solid and Fluid Mechanics, Oxford University Press, 1998.
[16] J.C. Butcher, On Runge-Kutta processes of high order, J. Aust. Math. Soc. 4 (2) (1964) 179–194.
[17] J.C. Butcher, A history of Runge-Kutta methods, Appl. Numer. Math. 20 (3) (1996) 247–260.
[18] J.C. Butcher, Numerical Methods for Ordinary Differential Equations, John Wiley & Sons, 2016.
[19] C.A. Kennedy, M.H. Carpenter, Diagonally Implicit Runge-Kutta Methods for Ordinary Differential Equations. A Review, Tech. Rep., National Aeronautics and Space Administration, NASA, 2016.
[20] L. Wan, C.A. Neumann, P.R. LeDuc, Tumor-on-a-chip for integrating a 3D tumor microenvironment: chemical and mechanical factors, Lab A Chip 20 (5) (2020) 873–888.
[21] T. Hillen, K.J. Painter, A user's guide to PDE models for chemotaxis, J. Math. Biol. 58 (1–2) (2009) 183–217.
[22] A. Agosti, P.F. Antonietti, P. Ciarletta, M. Grasselli, M. Verani, A cahn-hilliard–type equation with application to tumor growth dynamics, Math. Methods Appl. Sci. 40 (18) (2017) 7598–7626.
[23] A. Agosti, C. Giverso, E. Faggiano, A. Stamm, P. Ciarletta, A personalized mathematical tool for neuro-oncology: A clinical case study, Int. J. Non-Linear Mech. 107 (2018) 170–181.
[24] V. Mohammadi, M. Dehghan, S. De Marchi, Numerical simulation of a prostate tumor growth model by the RBF-FD scheme and a semi-implicit time discretization, J. Comput. Appl. Math. 388 (2021) 113314.
[25] V. Mohammadi, M. Dehghan, A. Khodadadian, N. Noii, T. Wick, An asymptotic analysis and numerical simulation of a prostate tumor growth model via the generalized moving least squares approximation combined with semi-implicit time integration, Appl. Math. Model. 104 (2022) 826–849.
[26] P. Colli, H. Gomez, G. Lorenzo, G. Marinoschi, A. Reali, E. Rocca, Mathematical analysis and simulation study of a phase-field model of prostate cancer growth with chemotherapy and antiangiogenic therapy effects, Math. Models Methods Appl. Sci. 30 (07) (2020) 1253–1295.
[27] J. Ayensa-Jiménez, M. Pérez-Aliacar, M.H. Doweidar, E.A. Gaffney, M. Doblaré, An overview from physically-based to data-driven approaches of the modelling and simulation of glioblastoma progression in microfluidic devices, Arch. Comput. Methods Eng. (2025) 1–37.
[28] Y.A. Yabo, S.P. Niclou, A. Golebiewska, Cancer cell heterogeneity and plasticity: A paradigm shift in glioblastoma, Neuro-Oncol. 24 (5) (2022) 669–682.
[29] D.J. Brat, E.G. Van Meir, Vaso-occlusive and prothrombotic mechanisms associated with tumor hypoxia, necrosis, and accelerated growth in glioblastoma, Lab. Invest. 84 (4) (2004) 397–405.
[30] M. Domènech, A. Hernández, A. Plaja, E. Martínez-Balibrea, C. Balañà, Hypoxia: the cornerstone of glioblastoma, Int. J. Mol. Sci. 22 (22) (2021) 12608.
[31] D. Balding, D.L.S. McElwain, A mathematical model of tumour-induced capillary growth, J. Theoret. Biol. 114 (1) (1985) 53–73.
[32] H. Byrne, Dissecting cancer through mathematics: from the cell to the animal model, Nat. Rev. Cancer 10 (3) (2010) 221–230.
[33] P. Kumar, M. Lacroix, P. Dupré, J. Arslan, L. Fenou, B. Orsetti, L. Le Cam, D. Racoceanu, O. Radulescu, Deciphering oxygen distribution and hypoxia profiles in the tumor microenvironment: a data-driven mechanistic modeling approach, Phys. Med. Biol. 69 (12) (2024) 125023.
[34] H. Hatzikirou, D. Basanta, M. Simon, K. Schaller, A. Deutsch, 'Go or grow': the key to the emergence of invasion in tumour progression? Math. Med. Biology: A J. the IMA 29 (1) (2012) 49–65.
[35] B. Stramer, R. Mayor, Mechanisms and in vivo functions of contact inhibition of locomotion, Nature Rev. Mol. Cell Biol. 18 (1) (2017) 43–55.
[36] A. Carreau, B. Hafny-Rahbi, A. Matejuk, C. Grillon, C. Kieda, Why is the partial oxygen pressure of human tissues a crucial parameter? Small molecules and hypoxia, J. Cell. Mol. Med. 15 (6) (2011) 1239–1253.
[37] U. Alon, An introduction to systems biology: design principles of biological circuits, in: An Introduction to Systems Biology: Design Principles of Biological Circuits, in: Chapman and Hall/CRC Mathematical & Computational Biology Series (10), Chapman & Hall/CRC, Boca Raton, Fla., 2006.
[38] A. Chauviere, L. Preziosi, H. Byrne, A model of cell migration within the extracellular matrix based on a phenotypic switching mechanism, Math. Med. Biology: A J. the IMA 27 (3) (2010) 255–281.
[39] K. Pham, A. Chauviere, H. Hatzikirou, X. Li, H.M. Byrne, V. Cristini, J. Lowengrub, Density-dependent quiescence in glioma invasion: instability in a simple reaction–diffusion model for the migration/proliferation dichotomy, J. Biol. Dyn. 6 (sup1) (2012) 54–71.
[40] A. Ern, J.-L. Guermond, Finite Elements III: First-Order and Time-Dependent PDEs, Springer, 2021, http://dx.doi.org/10.1007/978-3-030-57348-5, URL https://hal.science/hal-03226051.

[41] P. Colli, H. Gomez, G. Lorenzo, G. Marinoschi, A. Reali, E. Rocca, Mathematical analysis and simulation study of a phase-field model of prostate cancer growth with chemotherapy and antiangiogenic therapy effects, Math. Models Methods Appl. Sci. 30 (7) (2020) 1253–1295, http://dx.doi.org/10.1142/S0218202520500220, URL https://doi-org.recursos.biblioteca.upc.edu/10.1142/S0218202520500220.

[42] G. Papageorgiou, C. Tsitouras, Continuous extensions to high order Runge-Kutta methods, Int. J. Comput. Math. 65 (3–4) (1997) 273–291, http://dx.doi.org/10.1080/00207169708804616.

[43] T.S. Baker, J.R. Dormand, J.P. Gilmore, P.J. Prince, Continuous approximation with embedded runge-kutta methods, Appl. Numer. Math. 22 (1–3) (1996) 51–62, http://dx.doi.org/10.1016/S0168-9274(96)00025-6, Special issue celebrating the centenary of Runge-Kutta methods.

[44] R.D. Skeel, M. Berzins, A method for the spatial discretization of parabolic equations in one space variable, SIAM J. Sci. Stat. Comput. 11 (1) (1990) 1–32, http://dx.doi.org/10.1137/0911001.

[45] A. Gargallo-Peiró, X. Roca, J. Peraire, J. Sarrate, A distortion measure to validate and generate curved high-order meshes on CAD surfaces with independence of parameterization, Internat. J. Numer. Methods Engrg. 106 (13) (2016) 1100–1130.

[46] E. Ruiz-Gironés, A. Gargallo-Peiró, J. Sarrate, X. Roca, Automatically imposing incremental boundary displacements for valid mesh morphing and curving, Computer-Aided Des. 112 (2019) 47–62.

[47] D.I. Ketcheson, B. Seibold, D. Shirokoff, D. Zhou, DIRK schemes with high weak stage order, in: S.J. Sherwin, D. Moxey, J. Peiró, P.E. Vincent, C. Schwab (Eds.), Spectral and High Order Methods for Partial Differential Equations ICOSAHOM 2018, Springer International Publishing, Cham, 2020, pp. 453–463.